The Astronomical Journal, 163:79 (17pp), 2022 February https://doi.org/10.3847/1538-3881/ac3000

A 20 Second Cadence View of Solar-type Stars and Their Planets with TESS: Asteroseismology of Solar Analogs and a Recharacterization of π Men c

Daniel Huber[1], Timothy R. White[2,3], Travis S. Metcalfe[4], Ashley Chontos[1,41], Michael M. Fausnaugh[5], Cynthia S. K. Ho[6], Vincent Van Eylen[6], Warrick H. Ball[7,3], Sarbani Basu[8], Timothy R. Bedding[2,3], Othman Benomar[9,10], Diego Bossini[11], Sylvain Breton[12], Derek L. Buzasi[13], Tiago L. Campante[11,14], William J. Chaplin[7,3], Jørgen Christensen-Dalsgaard[3], Margarida S. Cunha[11,14], Morgan Deal[11,14], Rafael A. García[12], Antonio García Muñoz[12], Charlotte Gehan[11,15], Lucía González-Cuesta[16,17], Chen Jiang[15], Cenk Kayhan[18], Hans Kjeldsen[3,19], Mia S. Lundkvist[3], Stéphane Mathis[12], Savita Mathur[16,17], Mário J. P. F. G. Monteiro[11,14], Benard Nsamba[20,21,22], Jia Mian Joel Ong[8], Erika Pakštienė[19], Aldo M. Serenelli[23,24], Victor Silva Aguirre[3], Keivan G. Stassun[25,26], Dennis Stello[2,3,27], Sissel Norgaard Stilling[3], Mark Lykke Winther[3], Tao Wu[28,29,30,31], Thomas Barclay[32,33], Tansu Daylan[5,42], Maximilian N. Günther[5], J. J. Hermes[34], Jon M. Jenkins[35], David W. Latham[36], Alan M. Levine[5], George R. Ricker[5], Sara Seager[5,37,38], Avi Shporer[5], Joseph D. Twicken[35,39], Roland K. Vanderspek[5], and Joshua N. Winn[40]

[1] Institute for Astronomy, University of Hawai'i, 2680 Woodlawn Drive, Honolulu, HI 96822, USA; huberd@hawaii.edu
[2] Sydney Institute for Astronomy (SIfA), School of Physics, University of Sydney, NSW 2006, Australia
[3] Stellar Astrophysics Centre (SAC), Department of Physics and Astronomy, Aarhus University, Ny Munkegade 120, DK-8000 Aarhus C, Denmark
[4] White Dwarf Research Corporation, 9020 Brumm Trail, Golden, CO 80403, USA
[5] Department of Physics and Kavli Institute for Astrophysics and Space Research, Massachusetts Institute of Technology, 77 Massachusetts Avenue, Cambridge, MA 02139, USA
[6] Mullard Space Science Laboratory, University College London, Holmbury St Mary, Dorking, Surrey RH5 6NT, UK
[7] School of Physics and Astronomy, University of Birmingham, Birmingham B15 2TT, UK
[8] Department of Astronomy, Yale University, P.O. Box 208101, New Haven, CT 06520-8101, USA
[9] Center for Space Science, New York University Abu Dhabi, UAE
[10] Division of Solar and Plasma Astrophysics, NAOJ, Mitaka, Tokyo, Japan
[11] Instituto de Astrofísica e Ciências do Espaço, Universidade do Porto, CAUP, Rua das Estrelas, 4150-762 Porto, Portugal
[12] AIM, CEA, CNRS, Université Paris-Saclay, Université Paris Diderot, Sorbonne Paris Cité, F-91191 Gif-sur-Yvette, France
[13] Dept. of Chemistry & Physics, Florida Gulf Coast University, 10501 FGCU Boulevard South, Fort Myers, FL 33965 USA
[14] Departamento de Física e Astronomia, Faculdade de Ciências da Universidade do Porto, Rua do Campo Alegre, s/n, 4169-007 Porto, Portugal
[15] Max-Planck-Institut für Sonnensystemforschung, Justus-von-Liebig-Weg 3, D-37077 Göttingen, Germany
[16] Instituto de Astrofísica de Canarias (IAC), E-38205 La Laguna, Tenerife, Spain
[17] Universidad de La Laguna (ULL), Departamento de Astrofísica, E-38206 La Laguna, Tenerife, Spain
[18] Department of Astronomy and Space Sciences, Science Faculty, Erciyes University, 38030 Melikgazi, Kayseri, Turkey
[19] Institute of Theoretical Physics and Astronomy, Vilnius University, Sauletekio av. 3, 10257 Vilnius, Lithuania
[20] Max-Planck-Institut für Astrophysik, Karl-Schwarzschild-Str. 1, D-85748 Garching, Germany
[21] Instituto de Astrofísica e Ciências do Espaço, Universidade do Porto, Rua das Estrelas, PT4150-762 Porto, Portugal
[22] Kyambogo University, P.O. Box 1, Kyambogo Hill, Kampala, Uganda
[23] Institute of Space Sciences (ICE, CSIC) Campus UAB, Carrer de Can Magrans, s/n, E-08193, Barcelona, Spain
[24] Institut d'Estudis Espacials de Catalunya (IEEC), C/Gran Capita, 2-4, E-08034, Barcelona, Spain
[25] Vanderbilt University, Department of Physics & Astronomy, 6301 Stevenson Center Lane, Nashville, TN 37235, USA
[26] Vanderbilt Initiative in Data-intensive Astrophysics (VIDA), 6301 Stevenson Center Lane, Nashville, TN 37235, USA
[27] School of Physics, The University of New South Wales, Sydney, NSW 2052, Australia
[28] Yunnan Observatories, Chinese Academy of Sciences, 396 Yangfangwang, Guandu District, Kunming, 650216, People's Republic of China
[29] Key Laboratory for the Structure and Evolution of Celestial Objects, Chinese Academy of Sciences, 396 Yangfangwang, Guandu District, Kunming, 650216, People's Republic of China
[30] Center for Astronomical Mega-Science, Chinese Academy of Sciences, 20A Datun Road, Chaoyang District, Beijing, 100012, People's Republic of China
[31] University of Chinese Academy of Sciences, Beijing 100049, People's Republic of China
[32] NASA Goddard Space Flight Center, 8800 Greenbelt Road, Greenbelt, MD 20771, USA
[33] University of Maryland, Baltimore County, 1000 Hilltop Circle, Baltimore, MD 21250, USA
[34] Department of Astronomy & Institute for Astrophysical Research, Boston University, 725 Commonwealth Avenue, Boston, MA 02215, USA
[35] NASA Ames Research Center, Moffett Field, CA 94035, USA
[36] Center for Astrophysics | Harvard & Smithsonian, 60 Garden Street, Cambridge, MA 02138, USA
[37] Department of Earth, Atmospheric, and Planetary Sciences, Massachusetts Institute of Technology, 77 Massachusetts Avenue, Cambridge, MA 02139, USA
[38] Department of Aeronautics and Astronautics, Massachusetts Institute of Technology, 77 Massachusetts Avenue, Cambridge, MA 02139, USA
[39] SETI Institute, 189 Bernardo Avenue, Suite 200, Mountain View, CA 94043, USA
[40] Department of Astrophysical Sciences, Princeton University, 4 Ivy Lane, Princeton, NJ 08544, USA
Received 2021 August 20; revised 2021 October 12; accepted 2021 October 13; published 2022 January 20

[41] NSF Graduate Research Fellow.
[42] Kavli Fellow.

Abstract

We present an analysis of the first 20 second cadence light curves obtained by the TESS space telescope during its extended mission. We find improved precision of 20 second data compared to 2 minute data for bright stars when binned to the same cadence (≈10%–25% better for $T \lesssim 8$ mag, reaching equal precision at $T \approx 13$ mag), consistent with pre-flight expectations based on differences in cosmic-ray mitigation algorithms. We present two results enabled by this improvement. First, we use 20 second data to detect oscillations in three solar analogs (γ Pav, ζ Tuc, and π Men) and use asteroseismology to measure their radii, masses, densities, and ages to ≈1%, ≈3%, ≈1%, and ≈20% respectively, including systematic errors. Combining our asteroseismic ages with chromospheric activity measurements, we find evidence that the spread in the activity–age relation is linked to stellar mass and thus the depth of the convection zone. Second, we combine 20 second data and published radial velocities to recharacterize π Men c, which is now the closest transiting exoplanet for which detailed asteroseismology of the host star is possible. We show that π Men c is located at the upper edge of the planet radius valley for its orbital period, confirming that it has likely retained a volatile atmosphere and that the "asteroseismic radius valley" remains devoid of planets. Our analysis favors a low eccentricity for π Men c (<0.1 at 68% confidence), suggesting efficient tidal dissipation ($Q/k_{2,1} \lesssim 2400$) if it formed via high-eccentricity migration. Combined, these early results demonstrate the strong potential of TESS 20 second cadence data for stellar astrophysics and exoplanet science.

Unified Astronomy Thesaurus concepts: Exoplanets (498); G stars (558); Asteroseismology (73); Light curves (918); Transits (1711); Radial velocity (1332)

1. Introduction

Precise photometry of stars from space telescopes such as CoRoT (Baglin et al. 2006) and Kepler/K2 (Borucki et al. 2008; Howell et al. 2014) has revolutionized stellar astrophysics and exoplanet science over the past two decades. An important characteristic of light curves provided by these missions is the sampling rate (observing cadence), which limits the timescales of astrophysical variability that can be measured. For example, oscillations of Sun-like stars, white dwarfs, and rapidly oscillating Ap stars occur on timescales of minutes (Aerts et al. 2008; Handler 2013), requiring rapid sampling to unambiguously identify pulsation frequencies. While specialized techniques can be used to extract information above the Nyquist frequency (Murphy et al. 2013; Chaplin et al. 2014), shorter integration times also avoid amplitude attenuation caused by time-averaging and thus increase the signal-to-noise ratio (S/N). This is particularly important for Sun-like stars because they oscillate with low (≈parts-per-million) amplitudes (García & Ballot 2019). Fast sampling is also critical for resolving fast astrophysical transient phenomena such as stellar flares, which can occur on timescales of minutes (e.g., Hawley et al. 2014; Davenport 2016).

Rapid sampling is also important for transiting exoplanets. For example, resolving the duration of transit ingress and egress in combination with a precise mean stellar density allows breaking of degeneracies between impact parameter and orbital eccentricity (Seager & Mallén-Ornelas 2003; Winn et al. 2010; Dawson & Johnson 2012). This is particularly powerful for characterizing eccentricities—and thus dynamical formation histories—of small (sub-Neptune sized) planets (Van Eylen & Albrecht 2015; Xie et al. 2016), for which radial velocities often only provide weak eccentricity information. More broadly, constraints on impact parameters enabled by well-sampled light curves result in more accurate planet-to-star radius ratios, which in the era of Gaia (Gaia Collaboration et al. 2016) are sometimes the dominant factors in the error budgets of planet radii derived from transit photometry (Petigura 2020). Finally, high cadence also enables more accurate characterizations of transit-timing variations, which provide constraints on mass and eccentricity for small planets (e.g., Lissauer et al. 2011; Price & Rogers 2014).

Observing cadences for space telescopes are mostly set by limitations on onboard storage and bandwidth, which in turn are tied to the spacecraft orbit. Early missions such as MOST (Walker et al. 2003; Matthews et al. 2004), BRITE (Weiss et al. 2014), and CoRoT provided photometry with a cadence of less than a minute, but light-curve durations and precisions were limited by Sun-synchronous orbits, resulting in a small continuous viewing zone and significant contamination from stray light (e.g., Reegen et al. 2006). The Kepler mission mitigated both effects through an Earth-trailing orbit, providing continuous, long-duration photometry with high precision. However, the onboard storage capacity limited the observing cadence to 30 minute sampling (long-cadence) for the ≈165,000 main target stars (Jenkins et al. 2010), with a subset of 512 stars per observing quarter observed with 1 minute sampling (short-cadence, Gilliland et al. 2010). Kepler short-cadence observations demonstrated the value of rapid sampling, for example by enabling the first systematic program that takes advantage of the synergy between asteroseismology and exoplanet science (Huber et al. 2013a; Silva Aguirre et al. 2015; Davies et al. 2016; Lundkvist et al. 2016; Kayhan et al. 2019), and remained a highly sought after resource for the duration of the Kepler mission.

Thanks to its innovative orbit and large onboard storage, the NASA TESS mission (Ricker et al. 2014) is currently providing unprecedented flexibility for space-based, high-precision, and rapid photometry. During its two-year prime mission, TESS provided 30 minute cadence observations for the entire field of view and observed 20,000 preselected targets at 2 minute cadence for each observing sector.[43] In its extended mission, TESS also produces light curves with 20 second cadence, in addition to 2 minute cadence targets and 10 minute cadence full-frame images, providing new opportunities for asteroseismology and characterizing transiting planets. Here, we present an analysis of 20 second light curves obtained during the first sectors of the TESS extended mission, including an asteroseismic analysis of nearby solar analogs and

[43] TESS observed 16,000 targets in Sectors 1–3, after which the limit on the number of targets was increased to 20,000 stars.

a recharacterization of π Men c, the first transiting planet detected by TESS.

2. Observations

2.1. Target Sample

TESS currently observes 1000 stars per sector at 20 second cadence during the extended mission, 600 of which are selected through the TESS Guest Investigator and Directors Discretionary programs. Figure 1 shows an H-R diagram and stellar radius versus TESS magnitude for the ≈4900 unique stars with $T_{\rm eff} < 8000$ K observed during the first 10 sectors of the extended mission (2020 July 4 to 2021 April 2), using effective temperatures and radii from the TESS Input Catalog (Stassun et al. 2018, 2019). The TESS magnitude distribution in Figure 1(b) shows a pile-up at $T \approx 8$ mag, which predominantly corresponds to the 400 stars per sector observed for calibration purposes for the TESS Science Processing Operations Center (SPOC, Jenkins et al. 2016). The calibration stars are requested to be bright but unsaturated, resulting in a tendency toward more evolved red giant stars. The main-sequence sample consists of a large number of optically faint M dwarfs, which are monitored to study stellar flares (Günther et al. 2020; Feinstein et al. 2020), and a brighter sample of solar-type stars. Note that Figure 1 does not show compact stars (such as hot subdwarfs and white dwarfs), which are observed at 20 second cadence for asteroseismology (e.g., Bell et al. 2019; Charpinet et al. 2019) and to search for transiting planets (e.g., Vanderburg et al. 2020).

2.2. Photometric Performance

To test the photometric precision, we downloaded all 20 second light curves obtained in Sectors 27–36 from the Mikulski Archive for Space Telescopes (MAST). We used the PDC-MAP light curves provided by the SPOC, which have been optimized to remove instrumental variability (Smith et al. 2012; Stumpe et al. 2012, 2014). We performed standard data processing steps, retaining only data with quality flags set to zero. We then binned each light curve to 2 minute cadence and 60 minute cadence, high-pass filtered the data with a first-order 0.5 day Savitzky–Golay filter (Savitzky & Golay 1964), and calculated the standard deviation of the binned light curves (hereafter referred to as time-domain scatter) to provide a measure of the photometric precision on those timescales. We performed the same procedure using the original 2 minute light curves for the same stars, which are a standard SPOC data product and provide a benchmark for comparison to the new 20 second light curves. We calculated the photometric precision for each sector and each star to test the dependence of the noise properties on varying conditions between different sectors.

Figures 2(a) and (b) show the measured time-domain scatter for each star and each sector as a function of TESS magnitude over timescales of 2 minutes (left panels) and one hour (right panels). As expected, the noise increases toward fainter magnitudes due to photon, sky, and read noise. For each data set, we identified stars dominated by stellar variability by scaling the TESS noise model from Sullivan et al. (2015) upward by 40%, and marking all stars with a time-domain scatter above that level (gray points).

Figure 2 demonstrates that the 20 second light curves binned to 2 minute cadence show a strong magnitude-dependent improvement in precision compared to the original 2 minute cadence light curves. To illustrate this more clearly, Figure 2(c)

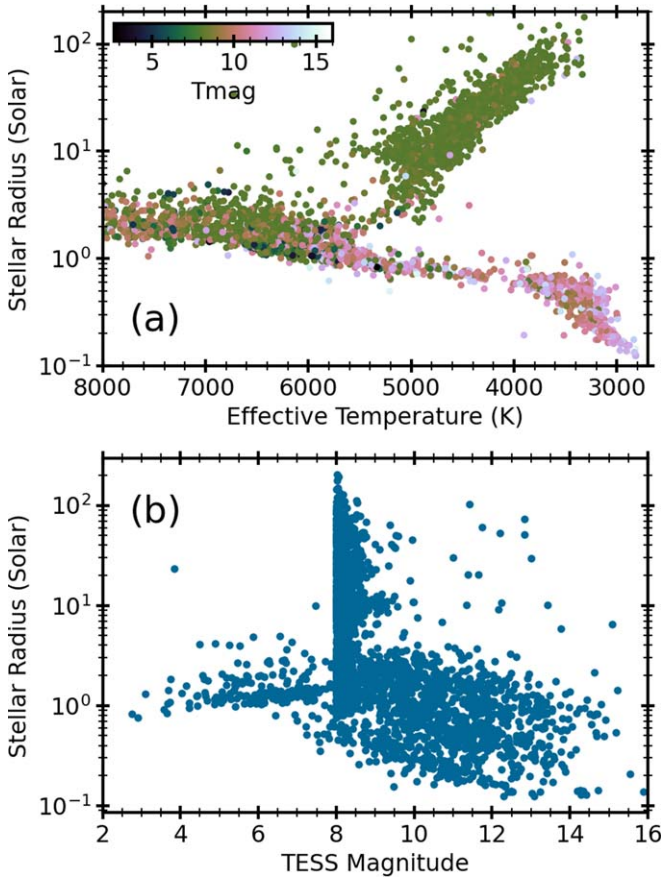

Figure 1. (a) Stellar radius versus effective temperature of the ≈4900 unique stars with $T_{\rm eff} < 8000$ K observed with TESS 20 second cadence observations during the first 10 sectors of the extended mission, color-coded by TESS magnitude T (capped at $T < 16$ mag). (b) Stellar radius versus TESS magnitude for the sample shown in panel (a). Compact stars (such as hot subdwarfs and white dwarfs) are excluded from both panels.

shows the ratio of the two measurements, again as a function of TESS magnitude. The average scatter for 20 second light curves is ≈25% lower at $T = 6$ mag, ≈10% lower at $T = 8$ mag, and reaches parity with the 2 minute light curves around $T = 13$ mag. The same effect is seen for light curves binned to 1 hr cadence (Figure 2(d)), but with larger scatter. Table 1 lists the median ratios in bins of one magnitude (orange circles in the bottom panels of Figure 2) for each data set, which may be used to approximate the precision of 20 second data relative to that of 2 minute data in the magnitude range $T = 6$–16 mag.

The improvement shown in Figure 2 can partially be explained by the difference in cosmic-ray rejection algorithms applied to 20 second and 2 minute data. Specifically, 20 second data do not undergo onboard cosmic-ray mitigation. Instead, cosmic-ray mitigation is performed through postprocessing by the SPOC, which identifies cadences affected by cosmic rays and attempts to correct their flux values. The onboard processing removes exposures with the highest and lowest flux for each stack of ten 2 second exposures, which leads to a 20% reduction in effective exposure time for 2 minute data (Vanderspek et al. 2018). This shorter effective exposure time would correspond to a precision penalty of ≈10% for 2 minute data if exposures were randomly rejected. Pre-flight simulations predicted a penalty closer to ≈3% after taking into account that only exposures with the lowest and highest flux values are rejected

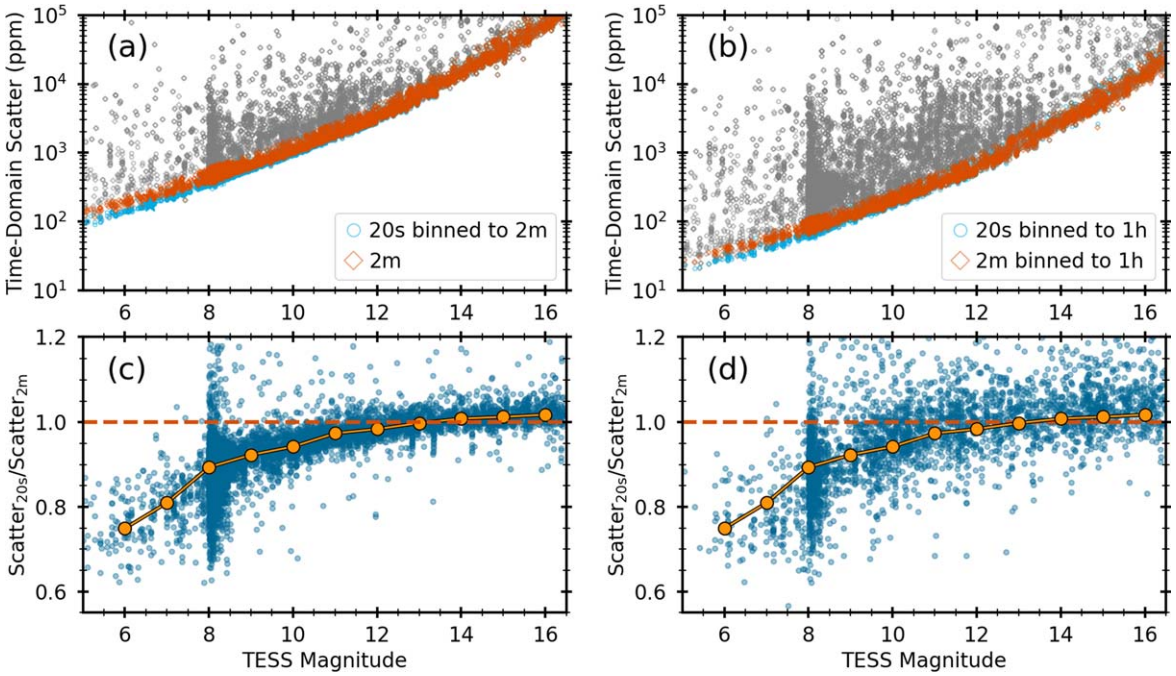

Figure 2. (a) Time-domain scatter as a function of TESS magnitude for stars observed in 20 second cadence between Sectors 27 and 36. Symbols show 20 second light curves binned to 2 minute cadence (cyan circles) and original 2 minute light curves (red diamonds) for each sector. Gray points mark stars likely dominated by stellar variability (see text). (b) Same as panel (a) but binning light curves to 1 hr cadence. (c) Ratio of the time-domain scatter for the two data sets shown in panel (a), retaining only stars not dominated by stellar variability (i.e., each point in panel (c) is the ratio of a cyan circle and red diamond in panel (a)). The dashed line marks unity and orange circles show median bins. (d) Same as panel (c) but for the binned light curves shown in panel (b).

Table 1
Noise Ratios between 20 second and 2 minute Data

TESS Magnitude	$[\sigma_{20s}/\sigma_{2m}]_{2m}$	$[\sigma_{20s}/\sigma_{2m}]_{1h}$
6.0	0.749 ± 0.007	0.766 ± 0.011
7.0	0.810 ± 0.005	0.771 ± 0.008
8.0	0.894 ± 0.001	0.877 ± 0.003
9.0	0.923 ± 0.002	0.925 ± 0.005
10.0	0.942 ± 0.002	0.955 ± 0.003
11.0	0.974 ± 0.001	0.985 ± 0.004
12.0	0.984 ± 0.001	0.996 ± 0.004
13.0	0.998 ± 0.001	1.006 ± 0.004
14.0	1.009 ± 0.001	1.012 ± 0.004
15.0	1.013 ± 0.001	1.027 ± 0.003
16.0	1.018 ± 0.002	1.032 ± 0.003

Note. Precision ratios apply for light curves retaining only quality flags set to zero. Keeping quality flags related to cosmic rays significantly degrades the 20 second data precision for bright stars (see text).

(Z. Berta-Thompson 2021, private communication). Since the improvement in Figure 2 is significantly larger than 3%, this implies that sources in addition to photon noise must contribute to the distribution.

One likely reason is pointing jitter, which for brighter stars should lead to larger changes in pixel values, which are then preferentially removed during the onboard cosmic-ray rejection for 2 minute data. To test this, we calculated time-domain scatter for the two halves of Sector 34, which had significantly different pointing performance. Figure 3 confirms that the second orbit of Sector 34, which has larger pointing jitter, shows a stronger improvement of 20 second compared to 2 minute data, especially for the brightest stars. The improvement becomes negligible for stars fainter than $T \approx 13$ mag.

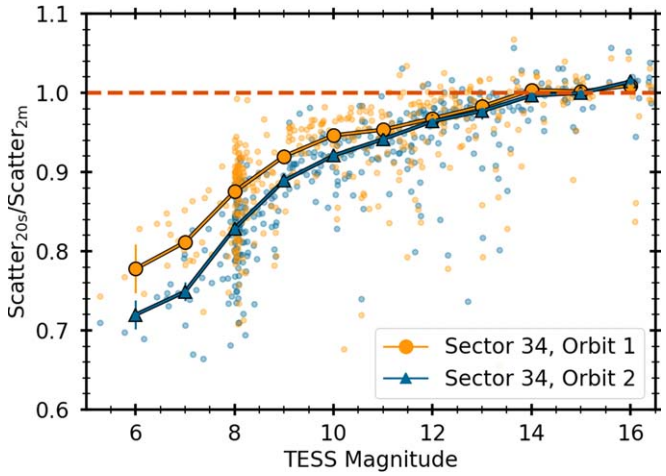

Figure 3. Ratio of the time-domain scatter for 20 second cadence data binned to 2 minute cadence and original 2 minute cadence light curves as a function of TESS magnitude for the first orbit (orange circles) and second orbit (blue triangles) of Sector 34 to test the impact of pointing jitter on the relative precision of the two light-curve products (see text). Filled symbols show median bins in steps of 1 mag. The dashed line marks unity.

We also repeated the calculations using three different quality-flag masks as defined in the Lightkurve package (v2.0.10): "Hardest" (rejecting all data with nonzero quality flags, as done above), "Hard" (rejecting data with severe and cosmic-ray flags only), and "Default" (rejecting data with severe flags only).[44] Figure 4 compares the ratio of the time-domain scatter for the three mask combinations. For 2 minute

[44] See https://github.com/nasa/Lightkurve/blob/master/lightkurve/utils.py. Note that the "Stray light" flag is currently not set in TESS 2 minute or 20 second data.

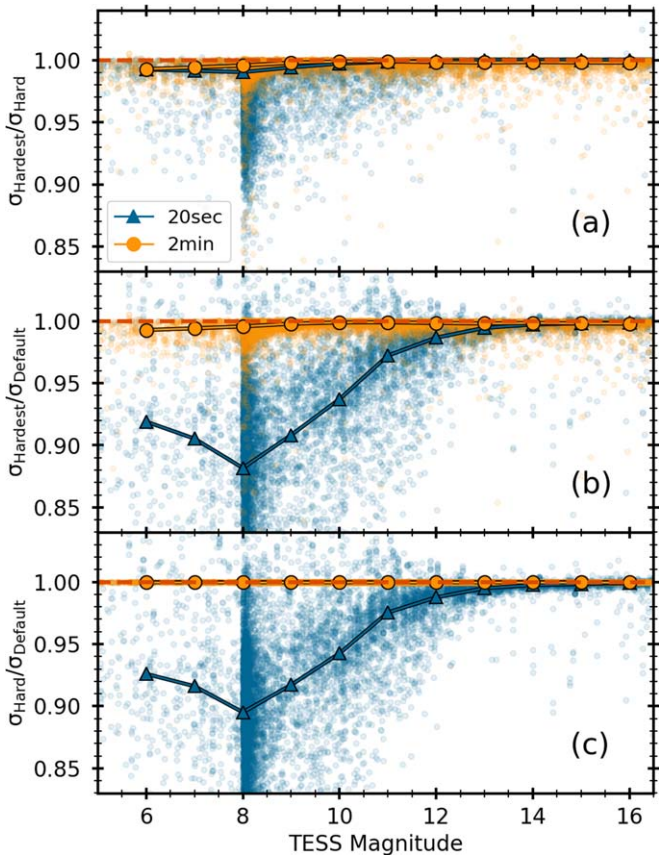

Figure 4. Ratio of the time-domain scatter for 20 second (blue triangles) and 2 minute (orange circles) data using three quality-flag masks as defined in the Lightkurve package: "Hardest" (rejecting all data with nonzero quality), "Hard" (rejecting severe and cosmic-ray flags), and "Default" (rejecting severe flags only). Points show individual sectors, filled symbols are median bins, and the dashed line marks unity.

data the mask choice has only a small impact ($\lesssim$1% on average) and yields identical results when comparing the "Hard" and "Default" masks due to the onboard cosmic-ray rejection. Removing data with cosmic-ray-related quality flags yields significantly lower noise for 20 second data, especially for bright stars ($T < 13$ mag). The shape of the distribution is similar to the bottom panels of Figure 2, demonstrating that removing cadences identified as cosmic rays during postprocessing is important for the improved precision of 20 second data for bright stars. For faint stars ($T > 13$ mag) the choice of quality-flag mask has little influence on the precision for 20 second cadence data, which implies that the corrections applied to cadences affected by cosmic rays during postprocessing are more efficient for faint stars. We conclude that on average the best photometric precision for 20 second data is achieved when keeping only quality flags set to zero for bright stars ($T < 13$ mag).

The results presented here were predicted in pre-flight simulations, which showed that spacecraft jitter would lead to excess noise when applying the onboard cosmic-ray mitigation for the brightest stars but would provide significant noise improvement for the larger number of faint stars (Z. Berta-Thompson, 2021, private communication). Additional effects that may impact the relative precision of 2 minute and 20 second light curves include the size of photometric apertures, which are calculated separately for each cadence. While a detailed investigation of these and other effects is left for future work, the confirmation of the pre-flight expectations presented here has significant ramifications for the allocation of 20 second cadence target slots, which are a scarce resource. Specifically, for stars brighter than $T < 13$ mag (and especially for $T < 8$ mag) 20 second data provide improved photometric precision irrespective of the timescale of astrophysical variability. Conversely, stars with $T > 13$ mag gain little from being observed in 20 second cadence unless the detection of astrophysical variability requires fast sampling (such as stellar flares or the detection of pulsations and transits for compact objects such as white dwarfs or subdwarfs).

3. Asteroseismology

3.1. Oscillations in Solar Analogs

To search for solar-like oscillations in the 20 second cadence sample, we analyzed all 84 solar-type stars observed as part of Cycle 3 Guest Investigator Program 3251[45] (PI Huber). We performed the same data processing steps described in the previous section and manually inspected the power spectra of each star. We only included data from Sectors 27 and 28 in this study.

We detected clear oscillations in three bright solar-like stars: γ Pav (F9V, $V = 4.2$ mag), ζ Tuc (F9.5V, $V = 4.2$ mag), and π Men (G0V, $V = 5.7$ mag). For π Men, the SPOC light curve for Sector 27 showed scatter that is about a factor of two larger than expected. We therefore constructed a custom light curve from the target pixel files using the Lightkurve software package (Lightkurve Collaboration et al. 2018). We selected a larger aperture than had been used to construct the SPOC light curve, thereby capturing more of the flux from π Men. The larger aperture was the single biggest factor in improving the quality of the light curve, and we confirmed that it captured all flux from saturated pixels. The light curve was extracted using simple aperture photometry. Then, to further correct for instrumental trends in the raw light curve, background pixels that were not within the target aperture were used to identify the four most significant trends via principal component analysis. The raw light curve was then detrended against these principal components, resulting in our corrected light curve. We created light curves for π Men and ζ Tuc using this method for both 20 second and 2 minute cadence data. For γ Pav we used regular SPOC PDC-MAP light curves.

Figure 5 shows the power spectrum of each star centered on the power excess due to solar-like oscillations. Note that we removed the transits of π Men c from the light curve prior to our analysis. The location of the power excess from oscillations predominantly depends on stellar surface gravity (Brown et al. 1991), and the observed excess at $\approx$2500 μHz for each star is consistent with predicted values from the TESS Asteroseismic Target List (ATL, Schofield et al. 2019). For comparison, the top panels of Figure 5 show power spectra calculated using the 2 minute cadence light curves of the same stars. We observe a strong improvement in S/N in all three stars, highlighting the benefit of the TESS 20 second light curve products for the study of solar-like oscillations in Sun-like stars. Indeed, this demonstrates that a few sectors of 2 minute data for π Men are insufficient for a detection of oscillations, which only become significant with 20 second cadence light curves.

[45] https://heasarc.gsfc.nasa.gov/docs/tess/data/approved-programs/cycle3/G03251.txt

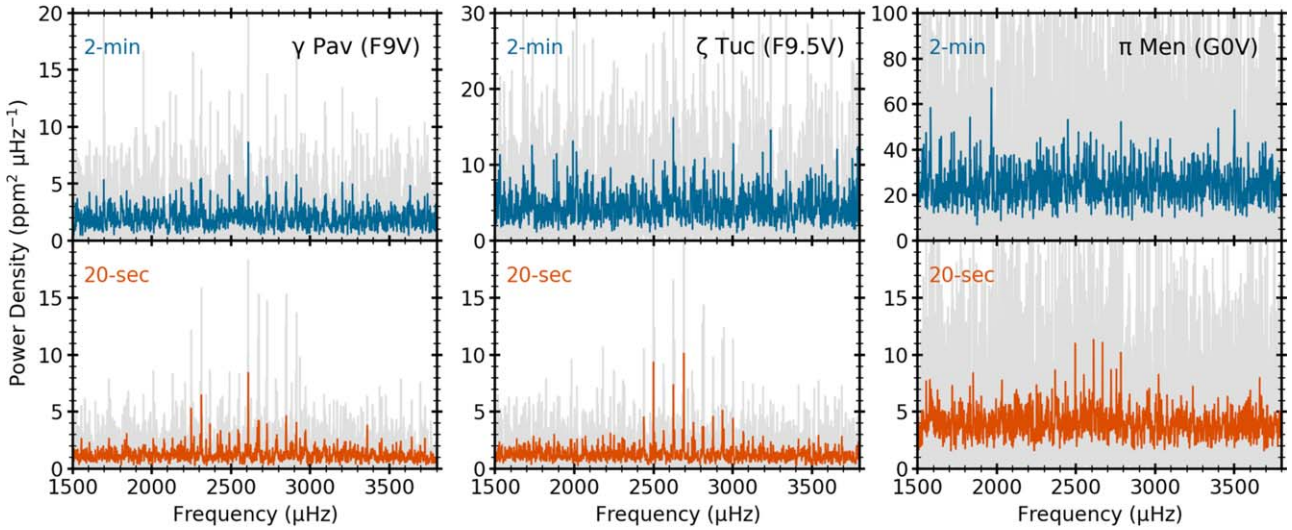

Figure 5. Power density spectra of the solar analogs γ Pav (left), ζ Tuc (middle), and π Men (right) calculated using original 2 minute cadence data (top) and 20 second cadence data (bottom). Gray lines show original power spectra, colored lines show power spectra smoothed by 2 μHz. The S/N of the detection dramatically increases for the 20 second cadence data.

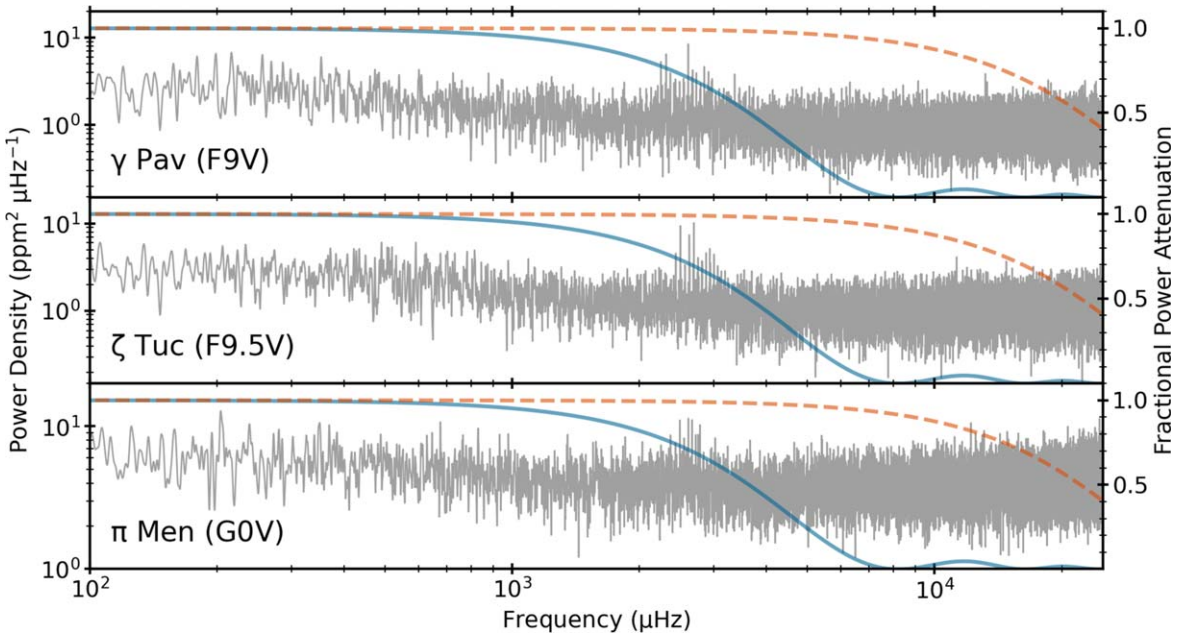

Figure 6. Power density spectra on a log–log scale using the 20 second cadence light curves for γ Pav (top), ζ Tuc (middle), and π Men (bottom). Each power spectrum was smoothed with a Gaussian with an FWHM of 1 μHz. Lines show the fractional power attenuation as given by Equation (2) on the right-hand y-axis for sampling at 2 minute cadence (solid lines) and 20 second cadence (dashed lines) in each panel.

In addition to the lower time-domain noise, the improvement in S/N in Figure 5 can be attributed to the reduced amplitude attenuation enabled by the shorter integration times of 20 second cadence observations. The fractional amplitude attenuation caused by time-averaging of a signal with frequency f is given by

$$A = \mathrm{sinc}(\pi f t_{\mathrm{exp}}), \tag{1}$$

where $\mathrm{sinc}(x) = (\sin x)/x$ and t_{exp} is the exposure time. For observations with no dead time between exposures, such as those obtained by TESS and Kepler, the exposure time is equal to the sampling time, and thus the fractional attenuation in power can be written as

$$P = \mathrm{sinc}^2\left(\frac{\pi}{2}\frac{f}{f_{\mathrm{Nyq}}}\right), \tag{2}$$

where $f_{\mathrm{Nyq}} = 1/(2\Delta t)$ is the Nyquist frequency for a time series with a constant sampling rate Δt.

Figure 6 shows the power spectra for the three stars on a log–log scale with lines showing the fractional power attenuation given by Equation (2). Figure 6 demonstrates that the longer sampling time of 2 minutes causes power attenuation of up to 30% at frequencies corresponding to the power excess of Sun-like stars. In contrast, the rapid sampling for 20 second cadence

alleviates power attenuation, demonstrating the importance of 20 second cadence data for the study of solar analogs using asteroseismology with TESS.

3.2. Power Spectrum Analysis

Several groups of coauthors used various methods of analysis to extract global oscillation parameters (e.g., Huber et al. 2009; Mosser & Appourchaux 2009; Mathur et al. 2010; Mosser et al. 2012a; Benomar et al. 2012; Corsaro & De Ridder 2014; Lundkvist 2015; Stello et al. 2017; Campante 2018; Nielsen et al. 2021; Chontos et al. 2021a), many of which have been extensively tested on Kepler, K2, and TESS data (e.g., Hekker et al. 2011; Verner et al. 2011; Zinn et al. 2020; Stello et al. 2021). In most of these analyses, the contributions due to granulation noise and stellar activity were modeled by a combination of Harvey-like functions (Harvey 1988) and a flat contribution due to photon noise. The frequency of maximum power ($\nu_{\rm max}$) was measured either by heavily smoothing the power spectrum or by fitting a Gaussian function to the power excess. We calculated final $\nu_{\rm max}$ values given in Table 5 as the median over a total of 11 different methods, with uncertainties calculated by adding in quadrature the standard deviations over all methods and the median formal uncertainty. The $\nu_{\rm max}$ measurement uncertainties range from $\approx$2% to 4%.

To extract individual frequencies, different groups of coauthors applied either traditional iterative sine-wave fitting, i.e., pre-whitening (e.g., Lenz & Breger 2005; Kjeldsen et al. 2005; Bedding et al. 2007) or Lorentzian mode-profile fitting (e.g., García et al. 2009; Handberg & Campante 2011; Appourchaux et al. 2012; Mosser et al. 2012b; Corsaro & De Ridder 2014; Corsaro et al. 2015, S. Breton 2021 in preparation). For each star, we compared results and required at least two independent methods to return the same frequency within uncertainties. For the final list of frequencies we adopted values from one fitter who applied pre-whitening, with uncertainties derived by adding in quadrature the median formal uncertainty and the standard deviation of the extracted frequencies from all methods that identified a given mode. The frequency lists are given in Tables 2, 3, and 4.

To measure the large frequency separation, $\Delta\nu$, we performed a weighted linear fit to all identified radial modes. Uncertainties were calculated by adding in quadrature the median formal uncertainty and the standard deviation for all estimates, yielding an average $\Delta\nu$ uncertainty of 0.8% (Table 5). Figure 7 shows the power spectra in échelle format (Grec et al. 1983) using these $\Delta\nu$ values, with extracted frequencies overlaid. As expected from Figure 5, the frequency extraction was most successful for γ Pav and ζ Tuc, yielding 6–7 dipole modes and strong constraints on the small frequency separation between modes with $l = 0$ and 2, which is sensitive to the gradient of sound speed near the core and thus stellar age (Christensen-Dalsgaard 1988). The S/N for π Men is lower due its fainter magnitude, but still allowed the extraction of several radial and nonradial modes. The offset of the $l = 0$ ridge in each échelle diagram, which is sensitive to the properties of the near-surface layers of the star (e.g., Christensen-Dalsgaard et al. 2014), is consistent with expectations from Kepler measurements for stars with similar $\Delta\nu$ and $T_{\rm eff}$ (White et al. 2011).

Table 2
Extracted Oscillation Frequencies and Mode Identifications for γ Pav

f (μHz)	σ_f (μHz)	l
2249.47	0.42	1
2305.83	0.86	2
2313.73	0.34	0
2367.90	0.58	1
2425.37	1.79	2
2433.42	0.70	0
2490.23	0.75	1
2545.02	0.89	2
2552.39	0.68	0
2609.23	0.48	1
2666.19	0.99	2
2672.37	1.04	0
2728.45	0.68	1
2783.03	1.53	2
2790.16	1.10	0
2849.84	0.84	1
2906.72	2.46	2
2912.60	1.14	0
2971.50	1.32	1

Table 3
Same as Table 2 but for ζ Tuc

f (μHz)	σ_f (μHz)	l
2439.55	0.46	0
2499.60	0.32	1
2558.06	0.99	2
2565.84	1.04	0
2625.23	0.41	1
2682.98	1.12	2
2691.73	0.49	0
2752.10	0.81	1
2809.75	0.61	2
2816.76	0.46	0
2876.80	0.44	1
2935.26	0.64	2
2944.52	0.72	0
3002.66	0.51	1
3069.40	1.04	0
3127.60	0.73	1

Table 4
Same as Table 2 but for π Men.

f (μHz)	σ_f (μHz)	l
2368.76	1.42	2
2433.31	0.86	1
2494.91	0.82	0
2550.41	0.78	1
2603.63	1.56	2
2611.63	1.21	0
2667.03	0.58	1
2721.50	1.11	2
2783.09	0.80	1

3.3. Classical Constraints

Due to the brightness of our stars, their atmospheric parameters such as effective temperature and metallicity have been extensively studied in the literature. We adopted $T_{\rm eff}$ and [Fe/H] from Aguilera-Gómez et al. (2018), which were homogeneously derived from high-resolution spectroscopy. These values fall within 1σ of the median of $T_{\rm eff}$ and [Fe/H]

Table 5
Stellar Parameters

	γ Pav	ζ Tuc	π Men
Hipparcos ID	1599	105858	26394
HD Number	203608	1581	39091
TIC ID	425935521	441462736	261136679
V_T magnitude	4.21	4.23	5.65
TESS magnitude	3.67	3.72	5.11
π (mas)	108.01 ± 0.11	116.18 ± 0.13	54.683 ± 0.035
$f_{\rm bol}$ (10^{-7} erg s^{-1} cm^{-2})	5.47 ± 0.18	5.34 ± 0.17	1.409 ± 0.058
L ($L_\odot$)	1.461 ± 0.049	1.232 ± 0.039	1.469 ± 0.061
$\nu_{\rm max}$(μHz)	2693 ± 95	2660 ± 99	2599 ± 69
$\Delta\nu$ (μHz)	119.9 ± 1.0	125.9 ± 0.8	116.7 ± 1.1
$T_{\rm eff}$ (K)	6168 ± 130	5924 ± 130	5980 ± 130
[Fe/H] (dex)	-0.66 ± 0.09	-0.21 ± 0.09	0.07 ± 0.07
$M_\star$ ($M_\odot$)	0.934 ± 0.021(ran) ± 0.026(sys)	0.985 ± 0.020(ran) ± 0.018(sys)	1.091 ± 0.026(ran) ± 0.016(sys)
$R_\star$ ($R_\odot$)	1.057 ± 0.008(ran) ± 0.009(sys)	1.044 ± 0.008(ran) ± 0.006(sys)	1.136 ± 0.009(ran) ± 0.006(sys)
$\rho_\star$ (g cm^{-3})	1.115 ± 0.004(ran) ± 0.014(sys)	1.222 ± 0.004(ran) ± 0.017(sys)	1.050 ± 0.003(ran) ± 0.013(sys)
$\log g$ (cgs)	4.359 ± 0.003(ran) ± 0.007(sys)	4.394 ± 0.003(ran) ± 0.006(sys)	4.365 ± 0.004(ran) ± 0.006(sys)
Age (Gyr)	5.9 ± 0.6(ran) ± 1.0(sys)	5.3 ± 0.5(ran) ± 0.2(sys)	3.8 ± 0.7(ran) ± 0.4(sys)

Note. V and TESS magnitudes are from the Tycho-2 catalog (Høg et al. 2000) and TESS Input Catalog (Stassun et al. 2018), and parallaxes are from Gaia EDR3 (Lindegren et al. 2021). Effective temperatures and metallicities are from Aguilera-Gómez et al. (2018), with uncertainties calculated as described in the text. All other quantities are determined in this work. For modeling γ Pav we adopted [M/H] $= -0.56 \pm 0.09$ dex based on α-element abundances in Bensby et al. (2005; see text).

from 15 to 30 independent studies based on both photometry and spectroscopy. We adopted a 2% systematic error in $T_{\rm eff}$, which accounts for uncertainties in the fundamental $T_{\rm eff}$ scale based on the accuracy of angular diameters measured using optical long-baseline interferometry (White et al. 2018; Tayar et al. 2020). This estimated uncertainty was added in quadrature to the formal 50 K spectroscopic errors.[46] We adopted a systematic uncertainty of 0.062 dex in [Fe/H] to account for method-specific offsets (Torres et al. 2012). Note that γ Pav is a metal-poor star with significant α-element enhancement of [α/Fe] $= 0.13 \pm 0.06$ dex, calculated using individual abundances from Bensby et al. (2005). Using the conversion by Salaris et al. (1993) yields [M/H] $= -0.56 \pm 0.09$ dex, which we adopted for model grids that do not specifically account for α-element enhancement.

To calculate bolometric fluxes ($f_{\rm bol}$), we fitted the spectral energy distribution of each target using broadband photometry following Stassun & Torres (2016). Independent estimates were calculated from Tycho V_T and B_T photometry (Høg et al. 2000), combined with bolometric corrections from MIST isochrones (Choi et al. 2016) as implemented in `isoclassify` (Huber et al. 2017). Interstellar extinction was found to be negligible in both methods, consistent with the short distances of all three targets. We also extracted $f_{\rm bol}$ estimates from the infrared flux method, as described in Casagrande et al. (2011). Our final $f_{\rm bol}$ estimates were calculated as the median over all methods, with uncertainties calculated by adding the mean uncertainty and scatter over all methods in quadrature. The final $f_{\rm bol}$ uncertainties are 3% to 4%, consistent with the expected systematic offsets (Zinn et al. 2019; Tayar et al. 2020). Finally, we combined $f_{\rm bol}$ values with Gaia EDR3 parallaxes (Lindegren et al. 2021) to calculate luminosities, which provide an independent constraint for asteroseismic modeling. The results are summarized in Table 5.

[46] All three stars have predicted angular diameters between ≈0.5 and 1 mas, which can be resolved with current optical long-baseline interferometers. Measuring these angular diameters would be valuable to reduce the systematic uncertainties on $T_{\rm eff}$.

3.4. Frequency Modeling

Different groups of coauthors used a number of approaches to model the observed oscillation frequencies, including different stellar evolution codes (ASTEC, GARSTEC, MESA, and YREC, Demarque et al. 2008; Christensen-Dalsgaard 2008; Weiss et al. 2008; Paxton et al. 2011, 2013, 2015; Choi et al. 2016), oscillation codes (including ADIPLS and GYRE, Antia & Basu 1994; Christensen-Dalsgaard 2008; Townsend & Teitler 2013), and modeling methods (including AIMS, AMP, ASTFIT, BeSSP, BASTA, PARAM, and YB, Metcalfe et al. 2009; Stello et al. 2009; Basu et al. 2010; Gai et al. 2011; Silva Aguirre et al. 2015; Creevey et al. 2017; Serenelli et al. 2017; Rodrigues et al. 2014, 2017; Ong et al. 2021; Ball & Gizon 2017; Mosumgaard et al. 2018; Rendle et al. 2019). The adopted methods applied corrections for the surface effect (Kjeldsen et al. 2008; Ball & Gizon 2014). Model inputs included the spectroscopic temperature and metallicity, individual frequencies, $\Delta\nu$, and luminosity. To investigate the effects of different input parameters, modelers were asked to provide solutions with and without taking into account the luminosity constraint from Gaia.

Overall, the modeling efforts yielded consistent results and we were able to provide adequate fits to the observed oscillation frequencies, as expected for stars with properties close to those of the Sun. The modeling results excluding and including the luminosity were consistent, demonstrating that there is no strong disagreement between the luminosity implied from asteroseismic constraints and that from Gaia. To make use of the most observational constraints, we used the set of nine modeling solutions that used $T_{\rm eff}$, [Fe/H], frequencies, and the luminosity as input parameters. From this set of solutions, we adopted the self-consistent set of stellar parameters derived using MESA following Ball & Gizon (2017), which showed the smallest difference to the median derived mass when averaged over all three stars.

Table 5 lists our final stellar parameters for each star. For properties derived from asteroseismology (radius, mass, density, surface gravity, and age) we quote random errors using the formal

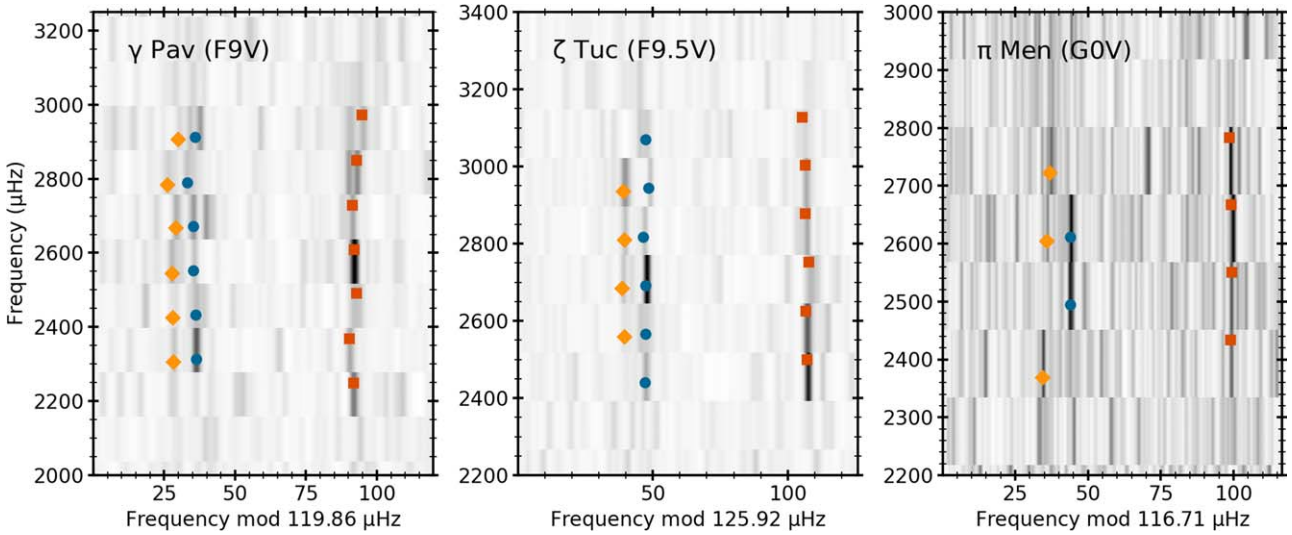

Figure 7. Échelle diagrams for γ Pav (left), ζ Tuc (middle), and π Men (right) using granulation-background corrected power spectra. Different symbols show measured radial modes (circles), dipole modes (squares), and quadrupole modes (diamonds). Error bars are smaller than symbol sizes in all cases.

uncertainty of the adopted method following Ball & Gizon (2017) and systematic errors as the standard deviation of the parameter over all methods. The results show that random and systematic errors make approximately equal contributions to the error budget, highlighting the importance of taking into account effects from different model grids. This is particularly pronounced for the mean stellar density, which formally can be measured with very high precision through the relation of the large separation to the integral of the sound speed (Ulrich 1986). The average uncertainties (calculated by adding random and systematic errors in quadrature) are ≈1% in radius, ≈3% in mass, ≈1% in density, and ≈20% in age, comparable to uncertainties from asteroseismology of Kepler stars (Silva Aguirre et al. 2017; Celik Orhan et al. 2021). Systematic age uncertainties are largest for γ Pav, consistent with larger differences in model predictions for metal-poor stars.

Mosser et al. (2008) presented an asteroseismic analysis of γ Pav based on five nights of radial velocity observations with HARPS. Our results show that the identification of even and odd degree modes was reversed in Mosser et al. (2008) due to the difficulty of ambiguously extracting frequencies from single-site ground-based data. Despite the different mode identification the derived mass is broadly compatible, but we measure a significantly younger age (5.9 Gyr compared to 7.3 Gyr). The younger age for γ Pav derived here is consistent with asteroseismic red giant populations that show a flat age–metallicity relation (and thus mostly constant star formation history) for stars in the Galactic disk (Casagrande et al. 2016; Silva Aguirre et al. 2018).

3.5. Activity–Age Relations

Magnetic activity cycles are one of the most poorly understood aspects of stellar evolution, but they play an important role in establishing empirical age indicators such as chromospheric activity (Mamajek & Hillenbrand 2008) and the spin-down of stars (gyrochronology, Barnes 2003). Stars with asteroseismic ages and characterized chromospheric activity cycles are critical ingredients for understanding and calibrating the interplay between rotation, age, and activity. The measurement of activity cycles requires decades-long observations,

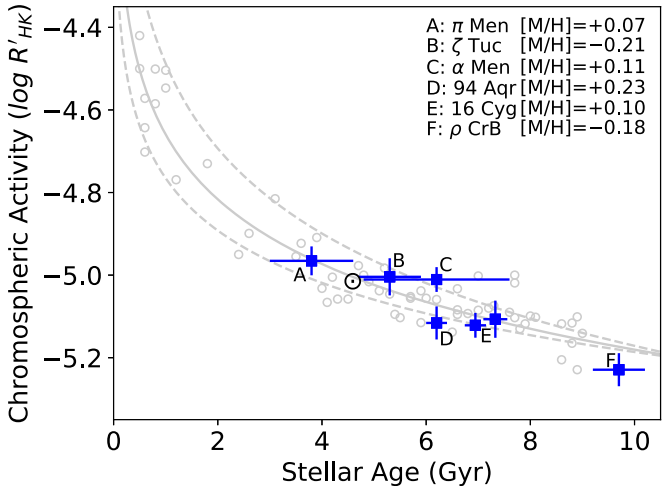

Figure 8. Chromospheric activity versus stellar age for a sample of spectroscopic solar twins from Lorenzo-Oliveira et al. (2018) with ages determined from isochrone fitting (gray circles). The fitted relation is shown as a solid line, with uncertainties indicated by dotted lines. Overplotted are bright stars with asteroseismic ages from TESS and Kepler (blue symbols).

which are typically only available for bright stars such as those included in the Mt. Wilson survey (Baliunas et al. 1995). TESS has already demonstrated this powerful synergy for the solar analog α Men (Chontos et al. 2021b) and the binary 94 Aqr (Metcalfe et al. 2020), thereby providing benchmarks for calibrating empirical age indicators.

The asteroseismic detections in bright solar analogs presented here provide additional benchmarks for calibrating activity–age relations. Figure 8 shows the activity–age relation for a sample of spectroscopic solar twins from Lorenzo-Oliveira et al. (2018) with measured chromospheric activity from Ca II H&K lines ($R'_{\rm HK}$) and ages derived through isochrone fitting. We overplot several bright stars with asteroseismic ages (Creevey et al. 2017; Chontos et al. 2021b; Metcalfe et al. 2020, 2021), including the solar analogs in this paper, with $R'_{\rm HK}$ placed on the same scale as Lorenzo-Oliveira et al. (2018) using the mean S-index values compiled by Boro Saikia et al. (2018) and the $T_{\rm eff}$ values in Table 5. The

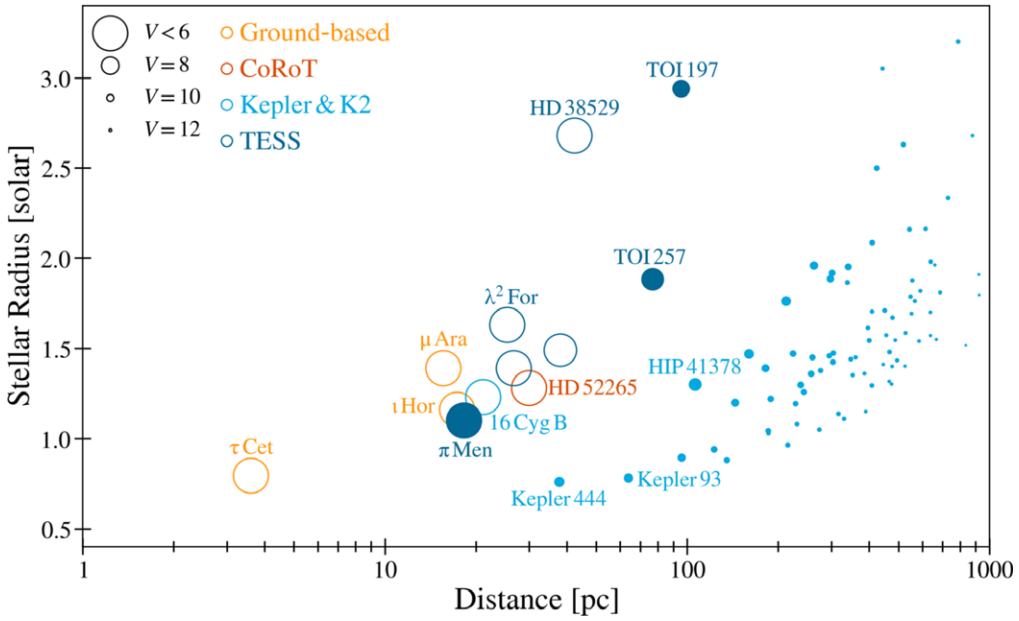

Figure 9. Stellar radius versus distance for the current population of asteroseismic host stars (excluding evolved stars with $R > 3.5\ R_{\odot}$) with confirmed $\Delta\nu$ measurements from ground-based radial velocity observations (orange), CoRoT (red), Kepler/K2 (light blue), and TESS (dark blue). Markers are sized by their visual magnitude and filled symbols show systems with known transiting planets. π Men is now the closest and brightest star with a transiting planet for which detailed asteroseismic modeling is possible. Label references (in order of proximity)—τ Cet (Teixeira et al. 2009), μ Ara (Bouchy et al. 2005), ι Hor (Vauclair et al. 2008), π Men (this work), 16 Cyg B (Metcalfe et al. 2012), λ^2 For (Nielsen et al. 2020), HD 52265 (Lebreton 2012; Escobar et al. 2012; Lebreton & Goupil 2014), Kepler-444 (Campante et al. 2015), HD 38529 (Ball et al. 2020), Kepler-93 (Ballard et al. 2014), TOI-257 (Addison et al. 2021), TOI-197 (Huber et al. 2019) and HIP 41378 (Vanderburg et al. 2016; Becker et al. 2019; Lund et al. 2019).

resulting $R'_{\rm HK}$ values were corrected for metallicity effects ($0.5 \times$ [M/H] following Saar & Testa 2012, private communication). We omitted γ Pav from the plot because its low metallicity falls outside the calibration range. Error bars for the Lorenzo-Oliveira et al. (2018) sample were omitted because they do not take into account systematic errors from different model grids, as was done for the asteroseismic sample.

Figure 8 shows that the asteroseismic sample covers the critical regime at old ages ($\gtrsim$3 Gyr) where the activity–age relation flattens. Interestingly, we observe that stars with similar ages and masses (such as the Sun and ζ Tuc) have similar $R'_{\rm HK}$ values, while stars with similar ages but significantly different masses (such as α Men A and 94 Aqr Aa, with 0.94 $M_{\odot}$ and 1.22 $M_{\odot}$) show a significant spread in $R'_{\rm HK}$. This implies that the spread in the activity–age relation is probably linked to a spread in stellar mass and thus the depth of the convection zone, analogous to the mass (or zero-age main-sequence temperature) dependence of gyrochronology relations (e.g., van Saders et al. 2016). Additional asteroseismic results from TESS 20 second data will be required to quantify such differential effects in activity–age relations. Additional extended mission observations in 20 s cadence will also help to decrease the error bars on asteroseismic ages by enabling the detection of a larger number of oscillation frequencies and will complement the existing database of active solar analogs already measured by Kepler (Salabert et al. 2016).

4. The π Men Planetary System

4.1. Asteroseismic Host Stars

π Men joins the population of ≈110 exoplanet host stars that have been characterized using asteroseismology (Figure 9). The majority of the sample comes from Kepler (Huber et al. 2013a; Lundkvist et al. 2016), which has led to important insights into demographics of small-planet radii and eccentricities (Van Eylen & Albrecht 2015; Van Eylen et al. 2018a, 2019) and their dynamical formation histories through the measurement of asteroseismic spin-axis inclinations (Huber et al. 2013b; Chaplin et al. 2013; Benomar et al. 2014; Lund et al. 2014; Campante et al. 2016; Kamiaka et al. 2019; Zhang et al. 2021). While the reanalyses of Kepler data and new data from the K2 mission have added some detections (Van Eylen et al. 2018b; Chontos et al. 2019; Lund et al. 2019), the number of asteroseismic host stars has stagnated over the past few years. Furthermore, similar to the general asteroseismic and host star sample, most Kepler stars are faint and distant and thus difficult to characterize using ground-based observations.

First results from TESS have already started to expand the population with detected oscillations in nearby exoplanet host stars, including newly discovered transiting exoplanets such as TOI-197 (Huber et al. 2019) and TOI-257 (Addison et al. 2021) and known exoplanet hosts (Campante et al. 2019; Nielsen et al. 2020). Ground-based radial velocity campaigns have yielded asteroseismic detections in some bright nearby exoplanet hosts including π Men (Kunovac Hodžić et al. 2021), but are generally limited to single-site observations, causing ambiguities in the mode identification. The detection of oscillations presented here makes π Men the closest and brightest star with a known transiting planet for which detailed asteroseismic modeling is possible, and highlights the strong potential of 20 second data to increase the asteroseismic host star sample.

4.2. Transit and Radial Velocity Fit

The 20 second cadence data provide an opportunity to recharacterize π Men c, the first transiting planet discovered by TESS (Huang et al. 2018). In particular, the asteroseismic constraints on stellar radius and mean density, both measured

with an *accuracy* of ≈1%, allow the opportunity to resolve degeneracies between eccentricity, impact parameter, and transit duration. This degeneracy often limits the accuracy of derived planet radii (Petigura 2020) and can provide a constraint on the orbital eccentricities of small planets (Van Eylen & Albrecht 2015; Van Eylen et al. 2019). In addition to the sub-Neptune sized π Men c, the system includes a massive, nontransiting substellar companion on an eccentric orbit with a period of ≈5.7 yr discovered using radial velocities (Jones et al. 2002).

We used `exoplanet` (v0.4.0; Foreman-Mackey et al. 2021) to perform a joint fit of the TESS 20 second light curve and archival radial velocities spanning over ≈20 yr from UCLES/AAT (Jones et al. 2002), HARPS (Gandolfi et al. 2018; Huang et al. 2018), CORALIE, and ESPRESSO (Damasso et al. 2020). We follow Damasso et al. (2020) in splitting the HARPS, CORALIE, and ESPRESSO data sets based on expected zero-point offsets, calculating nightly bins, and parameterizing separate offsets and jitter terms (σ) for each of the eight radial velocity (RV) data sets. We also added a linear RV trend to the model to account for unknown outer companions. The transit model was parameterized with a photometric zero-point offset, an extra photometric jitter term ($\sigma_{\rm TESS}$), conjunction times (T_0), orbital periods (P), impact parameters (b), quadratic limb darkening parameters (u_1, u_2), eccentricity parameters ($\sqrt{e}\sin\omega$, $\sqrt{e}\cos\omega$), mean stellar density ($\rho_\star$), and radius ratio ($R_{\rm p}/R_\star$). We included a Gaussian process (GP) using a single simple harmonic oscillator kernel, consisting of a timescale ($\rho_{\rm GP}$), amplitude ($\sigma_{\rm GP}$), and a fixed quality factor $Q = 1/\sqrt{2}$, to account for instrumental and stellar variability in the TESS light curve. For computational efficiency we only used 1 day chunks of the light curve centered on each transit. We used informative priors for the stellar mean density and radius based on the derived asteroseismic parameters (Table 5) and wide Gaussian priors for the quadratic limb darkening parameters to account for uncertainties in model atmosphere predictions. The final model has 36 parameters, which were sampled using four chains with 1500 draws each and tested for convergence using the standard Gelman–Rubin statistic. The priors and summary statistics for our joint transit and RV model are listed in Table 6. Our results agree well with previous analyses of the π Men system (e.g., Damasso et al. 2020; Günther & Daylan 2021), but provide significantly improved eccentricity constraints for π Men c (see Section 4.3).

Figure 10 shows the phase-folded transit light curve for π Men c, and Figure 11 shows the radial velocity data for π Men b and c with best-fitting models. Figure 10 illustrates that the transits are well sampled in 20 second data, while 30 minute cadence would significantly smear out the durations of ingress and egress. A detailed comparison of 20 second compared to 2 minute cadence data for deriving transit parameters will be presented in a future study (C. S. K. Ho et al. 2021, in preparation). As demonstrated by Damasso et al. (2020), the combination of long baseline and high precision (in particular from ESPRESSO) for the available radial velocity data set provides exquisite constraints on both planets (Figure 11). We measure the radius and mass of π Men c to ≈2% and ≈13%, which include systematic errors on stellar parameters.

Table 6
π Men Planet Parameters

Parameter	Prior	Value
$T_{0,\rm b}$ (BTJD)	$\mathcal{N}(-466.8, 1.0)$	$-463.99^{+0.78}_{-0.76}$
$T_{0,\rm c}$ (BTJD)	$\mathcal{N}(1519.8, 0.1)$	$1519.8016^{+0.0086}_{-0.0085}$
$P_{\rm b}$ (days)	$\mathcal{N}(2090, 10)$	$2089.17^{+0.40}_{-0.40}$
$P_{\rm c}$ (days)	$\mathcal{N}(6.27, 0.01)$	$6.26789^{+0.0001}_{-0.0001}$
$\rho_\star$	$\mathcal{N}(1.050, 0.013)$	$1.052^{+0.013}_{-0.013}$
$\sqrt{e_{\rm b}}\cos\omega_{\rm b}$	$\mathcal{U}(-1, 1)$	$0.7039^{+0.0015}_{-0.0014}$
$\sqrt{e_{\rm b}}\sin\omega_{\rm b}$	$\mathcal{U}(-1, 1)$	$-0.3863^{+0.0036}_{-0.0033}$
$\sqrt{e_{\rm c}}\cos\omega_{\rm c}$	$\mathcal{U}(-1, 1)$	$0.014^{+0.170}_{-0.172}$
$\sqrt{e_{\rm c}}\sin\omega_{\rm c}$	$\mathcal{U}(-1, 1)$	$0.06^{+0.251}_{-0.251}$
$b_{\rm c}$	$\mathcal{U}(0, 1)$	$0.591^{+0.056}_{-0.144}$
u_1	$\mathcal{N}(0.28, 0.2)$	$0.30^{+0.12}_{-0.12}$
u_2	$\mathcal{N}(0.28, 0.2)$	$0.22^{+0.15}_{-0.15}$
$R_{\rm p}/R_\star$	$\mathcal{U}(0, 1)$	$0.01716^{+0.00024}_{-0.00030}$
$K_{\rm b}$ (m s^{-1})	$\mathcal{N}(200, 20)$	$194.55^{+2.83}_{-2.73}$
$K_{\rm c}$ (m s^{-1})	$\mathcal{N}(1.5, 1.5)$	$1.48^{+0.21}_{-0.20}$
$\sigma_{\rm GP}$ (ppm)	IG(3, 500)	$51.1^{+10.9}_{-8.0}$
$\rho_{\rm GP}$ (days)	$\log\mathcal{N}(5, 10)$	$2.61^{+0.89}_{-0.64}$
$\sigma_{\rm TESS}$ (ppm)	$\log\mathcal{N}(0, 10)$	$111.6^{+1.8}_{-1.8}$
$\sigma_{\rm AAT}$ (m s^{-1})	$\mathcal{U}(0.1, 100)$	$4.46^{+1.16}_{-0.98}$
$\sigma_{\rm HARPS_{pre}}$ (m s^{-1})	$\mathcal{U}(0.1, 100)$	$2.72^{+0.35}_{-0.30}$
$\sigma_{\rm HARPS_{post}}$ (m s^{-1})	$\mathcal{U}(0.1, 100)$	$2.30^{+0.20}_{-0.17}$
$\sigma_{\rm CORALIE_{98}}$ (m s^{-1})	$\mathcal{U}(0.1, 100)$	$13.13^{+4.53}_{-3.03}$
$\sigma_{\rm CORALIE_{07}}$ (m s^{-1})	$\mathcal{U}(0.1, 100)$	$11.54^{+3.45}_{-2.42}$
$\sigma_{\rm CORALIE_{14}}$ (m s^{-1})	$\mathcal{U}(0.1, 100)$	$4.29^{+0.84}_{-0.75}$
$\sigma_{\rm ESPRESSO_{pre}}$ (m s^{-1})	$\mathcal{U}(0.1, 100)$	$1.04^{+0.40}_{-0.27}$
$\sigma_{\rm ESPRESSO_{post}}$ (m s^{-1})	$\mathcal{U}(0.1, 100)$	$1.34^{+0.24}_{-0.20}$
Derived parameters for π Men b		
$e_{\rm b}$	⋯	$0.6447^{+0.0011}_{-0.0012}$
$\omega_{\rm b}$	⋯	$-28.75^{+0.27}_{-0.25}$
$a_{\rm b}/R_\star$	⋯	$625.6^{+2.5}_{-2.5}$
$a_{\rm b}$ (au)	⋯	$3.315^{+0.031}_{-0.031}$
$M\sin i_{\rm b}$ ($M_{\rm J}$)	⋯	$9.99^{+0.19}_{-0.19}$
$M_{\rm b}$ ($M_{\rm J}$)	⋯	$13.07^{+1.16}_{-0.87}$
Derived parameters for π Men c		
$e_{\rm c}$	⋯	$0.066^{+0.086}_{-0.047}$
$\omega_{\rm c}$	⋯	$38.7^{+78.0}_{-135.2}$
$a_{\rm c}/R_\star$	⋯	$12.977^{+0.052}_{-0.052}$
$a_{\rm c}$ (au)	⋯	$0.06876^{+0.00065}_{-0.00065}$
$i_{\rm c}$ (deg)	⋯	$87.37^{+0.40}_{-0.11}$
$R_{\rm c}$ ($R_\oplus$)	⋯	$2.131^{+0.037}_{-0.042}$
$M_{\rm c}$ ($M_\oplus$)	⋯	$4.50^{+0.66}_{-0.63}$

Note. See text for a description of all parameters. Nuisance parameters (photometric and RV instrument offsets, linear RV trend) are omitted from the table. $\mathcal{N}$, $\mathcal{U}$, and IG denote normal, uniform, and inverse gamma distributions. The mass of π Men b was calculated using $i = 49.^{\circ}9 \pm 5.^{\circ}0$ (De Rosa et al. 2020).

4.3. Dynamical Architecture

Orbital eccentricities, inclinations, and obliquities provide valuable information to constrain formation scenarios for close-in exoplanets. In particular, they help to distinguish dynamically "hot" formation pathways such as high-eccentricity migration triggered by planet–planet scattering (Chatterjee et al. 2008; Nagasawa et al. 2008) or Kozai–Lidov cycles (Kozai 1962; Lidov 1962; Fabrycky & Tremaine 2007) from in situ formation or migration in the protoplanetary disk (Cossou et al. 2014). While dynamical architectures have been

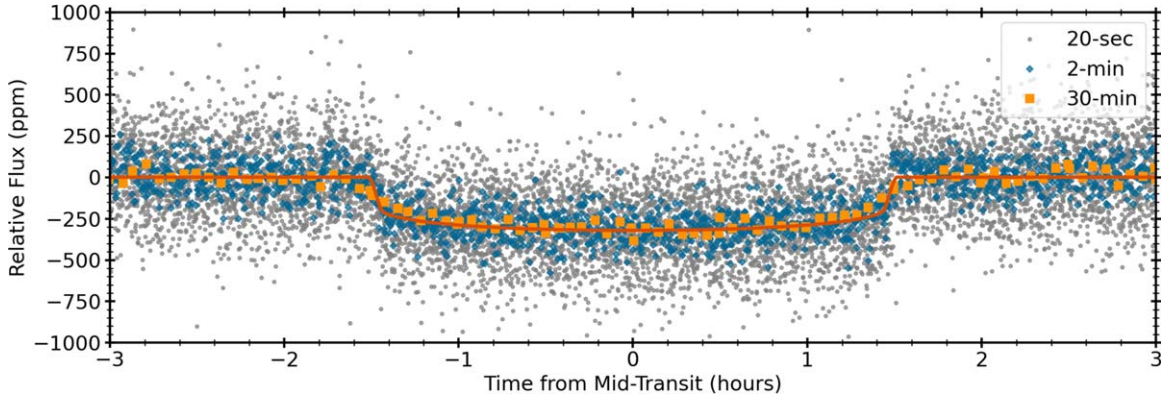

Figure 10. Phase-folded transit light of π Men c using 20 second data from Sectors 27 and 28 after removal of a Gaussian process model to account for trends due to stellar and instrumental effects. Diamonds and squares show the original 20 second cadence data (gray circles) binned into 2 minute and 30 minute cadence. The best-fitting transit model is shown as the solid line.

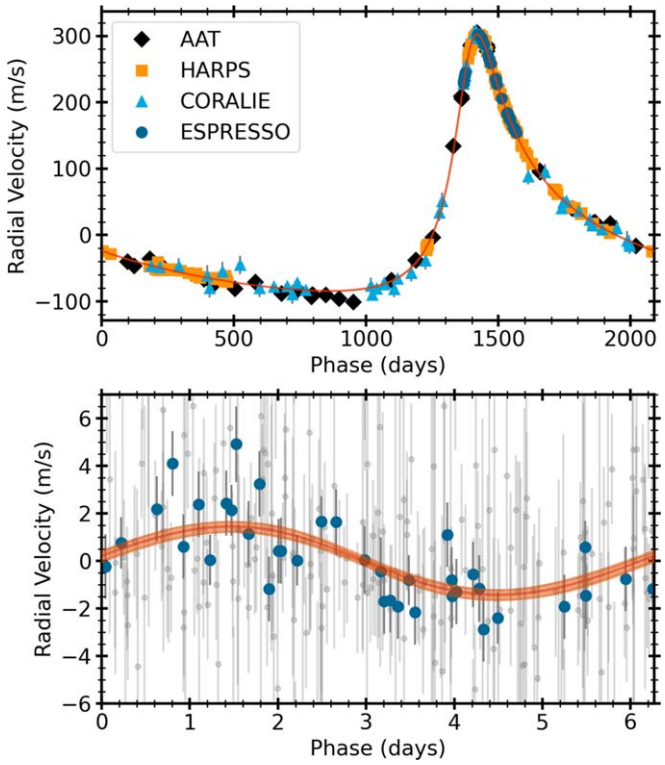

Figure 11. Radial velocity data phase-folded to the orbital periods of π Men b (top panel) and π Men c (bottom panel). The bottom panel shows all instruments except for ESPRESSO in gray. Each panel shows the RV data with the contribution from the other planet removed.

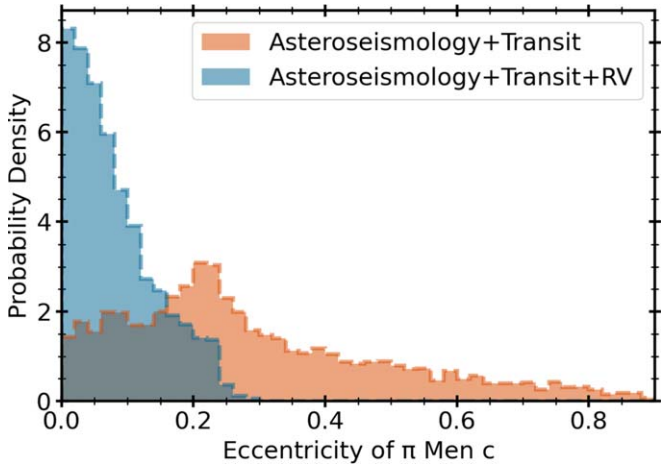

Figure 12. Marginalized posterior distribution on the orbital eccentricity of π Men c based on the 20 second cadence transit fitting with asteroseismic stellar parameters alone (red) and including information from radial velocities (blue).

extensively studied for hot Jupiters (e.g., Winn et al. 2010; Albrecht et al. 2012), constraints for sub-Neptune sized planets are still relatively scarce, in particular for systems with known outer companions (Rubenzahl et al. 2021).

π Men provides an excellent opportunity to study the dynamical formation pathway for a close-in sub-Neptune sized planet. The combination of Hipparcos and Gaia astrometry recently revealed that the orbit of π Men b is misaligned with that of π Men c (De Rosa et al. 2020; Xuan & Wyatt 2020), while Rossiter–McLaughlin observations show a $24^\circ \pm 4^\circ$ projected obliquity between the host star and π Men c (Kunovac Hodžić et al. 2021). Taken together these observations provide evidence for a dynamically hot formation pathway for π Men c. However, key dynamical properties such as the orbital eccentricity of π Men c have so far been poorly constrained.

Figure 12 shows the marginalized posterior distribution for the eccentricity of π Men c derived from our fit to the 20 second photometry alone, and also using the joint transit and RV fit. Both are consistent with a low eccentricity for π Men c, and the joint fit places an upper limit of <0.1 (68%), a factor of two tighter than previous constraints (Damasso et al. 2020). The posterior mode is consistent with a circular orbit, which implies that any initially high eccentricity caused by a dynamically hot formation has been damped over the 3.8 ± 0.8 Gyr lifetime of the system. Tidal dissipation rates are highly uncertain, mainly owing to the unknown planetary tidal quality factor (Q) and tidal Love number ($k_{2,1}$), which quantify the strength of the energy dissipation of tides in the planet and the perturbation of the gravitational potential at its surface due to star–planet tidal interactions (Ogilvie 2014; Mathis 2018). Assuming that π Men c has tidally circularized, we can place an upper limit on $Q/k_{2,1}$ assuming equilibrium tides (Goldreich & Soter 1966; Hut 1981; Xuan & Wyatt 2020):

$$\frac{Q}{k_{2,1}} < \frac{21\pi}{2}\frac{M_\star}{M_c}\left(\frac{R_c}{a_c}\right)^5 \frac{\tau}{P_c}, \quad (3)$$

where τ is the age of the star and P_c is the orbital period of π Men c. Substituting values from Tables 5 and 6, we arrive at $Q/k_{2,1} \lesssim 2400$. Assuming that π Men c has a rocky core composed of iron and silicates in terrestrial proportions with a radius of $\approx 1.5\ R_\oplus$ and a mass of $\approx 4.5\ M_\oplus$ as inferred from planetary interior modeling (García Muñoz et al. 2021), the ab initio computations by Tobie et al. (2019) imply $k_{2,1} \approx 0.4$ for π Men c (compared to 0.3 for the Earth, Wahr 1981). Using $Q/k_{2,1} \lesssim 2400$ leads to $Q \lesssim 970$, consistent with predictions that a $\approx 4.5\ M_\oplus$ planet with a terrestrial iron proportion should have $200 < Q < 1000$ depending on the considered viscosity (Tobie et al. 2019).

If π Men c arrived at its present-day configuration through high-eccentricity migration, as suggested by the orbital misalignments, our data imply that it has completed tidal circularization. Assuming that the eccentricity excitation occurred through Kozai–Lidov cycles with π Men b, this result would imply a present-day mutual inclination of π Men c to π Men b of $\sim 40^\circ$ or $\sim 140^\circ$ (De Rosa et al. 2020). Furthermore, the circular orbit would suggest that π Men c is not undergoing low-eccentricity migration, which has been suggested as a possible formation pathway for producing ultrashort-period planets (Pu & Lai 2019). Finally, the results imply that circular orbits for close-in sub-Neptune sized planet cannot be used to rule out dynamically hot formation scenarios. However, we note that dynamically "cold" formation pathways, such as disk migration or in situ formation, can still explain the observed properties of π Men c and thus cannot be completely excluded.

A key dynamical constraint for the π Men system is the inclination of the stellar spin axis, which would yield the full 3D architecture of the system. While the current S/N is insufficient to reliably measure this inclination using asteroseismology (Gizon & Solanki 2003; Ballot et al. 2006; Kamiaka et al. 2018), additional TESS 20 second observations (especially beyond the current extended mission, enabling >1 yr coverage) may enable some constraints on this important parameter.

4.4. Planet Radius Valley

The dearth of planets with radii around $1.8\ R_\oplus$ in the Kepler sample (Fulton et al. 2017) has sparked several efforts to investigate the origin and evolution of close-in sub-Neptune sized planets, including studies of small planets in the K2 sample (Hardegree-Ullman et al. 2020) and the dependence of the radius valley on both stellar mass (Fulton & Petigura 2018; Cloutier & Menou 2020; Van Eylen et al. 2021) and age (Berger et al. 2020; David et al. 2021; Sandoval et al. 2021). A remarkable feature of the radius valley is that it is devoid of planets for a sample of well characterized stars and planets using asteroseismology (Van Eylen et al. 2018a), suggesting that the dominant formation mechanism may be a relatively rapid process such as photoevaporation (Owen & Wu 2017). While there is evidence that many "gap planets" in the general Kepler sample are linked to underestimated uncertainties in transit fits from long-cadence photometry (Petigura 2020), recent studies have shown evidence for a transition of sub-Neptune to super-Earth sized planets on gigayear timescales (Berger et al. 2020) and a shift in the radius gap with stellar age (David et al. 2021), consistent with slower processes such as core-powered mass loss (Ginzburg et al. 2018; Gupta & Schlichting 2020). If the primary mechanism for sculpting the radius gap operates on gigayear timescales, we should find examples of old planets with ages similar to π Men c that are currently located in the gap.

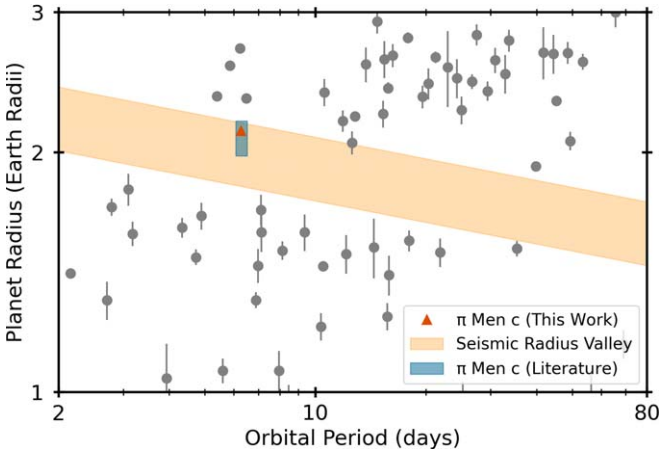

Figure 13. Planet radius versus orbital period for Kepler exoplanets orbiting asteroseismic host stars from Van Eylen et al. (2018a). The shaded area shows the best-fit model for the radius gap as a function of orbital period from Van Eylen et al. (2018a). The rectangle covers published radii (including 1σ uncertainties) for π Men c in the literature. The triangle marks the position of π Men c from our analysis, with the error bar being smaller than the symbol size.

Figure 13 compares our measured radius for π Men c with the sample of small planets orbiting asteroseismic Kepler stars from Van Eylen et al. (2018a). Unlike some other studies, our analysis firmly places π Men c at the upper edge of the radius gap at its orbital period. This confirms previous results that π Men c has probably held on to a significant volatile envelope even after 3.8 Gyr and is consistent with recent Hubble Space Telescope transmission spectroscopy as well as planetary interior and long-term evolution modeling, which imply that π Men c has an atmosphere of moderate to high molecular weight (García Muñoz et al. 2020, 2021).

The position of π Men c at the upper edge of the radius gap also confirms the lack of genuine "gap planets" in the asteroseismic host star sample. Since the asteroseismic sample is biased toward older solar-type stars with ages ranging from $\approx$2–12 Gyr and contains planets with well characterized radii, this suggests that the evolution of the radius valley may be restricted to $\lesssim$2 Gyr. However, we note that, depending on the actual composition of its core and envelope, it is also possible that π Men c will eventually evolve through the radius gap.

5. Conclusions

We have presented an analysis of the new 20 second cadence light curves provided by the TESS space telescope in its first extended mission. Our main conclusions are as follows.

1. TESS 20 second light curves show $\approx$10%–25% better precision than 2 minute light curves for bright stars with $T \lesssim 8$ mag, reaching equal precision at $T \approx 13$ mag. The improved precision is consistent with pre-flight expectations and can partially be explained by the increased effective exposure time for 20 second data due to the lack of onboard cosmic-ray rejection and the decreased efficiency of the onboard cosmic-ray rejection for 2 minute data in bright stars due to spacecraft pointing jitter. The results imply that TESS 20 second data are

particularly valuable for bright stars since they yield improved photometric precision irrespective of the timescale of astrophysical variability.

2. We use 20 second data to detect oscillations in three bright solar analogs observed in Sectors 27 and 28: γ Pav (F9V, $V = 4.2$), ζ Tuc (F9.5V, $V = 4.2$), and π Men (G0V, $V = 5.7$). We used asteroseismology to measure their radii to $\approx$1%, masses to $\approx$3%, densities to $\approx$1%, and ages to $\approx$20%, including systematic errors estimated by using different model grids and methods. We combine our asteroseismic ages with chromospheric activity measurements and find evidence that the spread in the activity–age relation is linked to stellar mass and thus the depth of the convection zone.
3. We combined asteroseismic stellar parameters, 20 second transit data, and published radial velocities to recharacterize π Men c, which is now the closest transiting exoplanet for which detailed asteroseismic characterization of the host star is possible. We measured the radius ($R = 2.13 \pm 0.04$ $R_\oplus$) and mass ($M = 4.5 \pm 0.6$ $M_\oplus$) to 2% and 13%, respectively. Our results show that π Men c sits at the upper edge of the planet radius valley, suggesting that it has probably held on to a volatile atmosphere. The planet radius valley, considering only exoplanets orbiting $\approx$2–12 Gyr old solar-type stars for which the precise asteroseismic characterization has been possible, remains devoid of planets.
4. Our analysis provides strong evidence for a circular orbit for π Men c ($e < 0.1$ at 68% confidence, with a mode consistent with zero). If π Men c arrived at its present orbit through high-eccentricity migration, as suggested by its misalignment with the outer substellar companion π Men b and the host star, our results imply that it has efficiently completed tidal circularization ($Q/k_{2,1} \lesssim 2400$ for the asteroseismic system age of 3.8 ± 0.8 Gyr) and that circular orbits for close-in sub-Neptune sized planets alone cannot be used to rule out dynamically hot formation scenarios.

Continued 20 second cadence observations in the TESS extended mission would yield the opportunity for an asteroseismic catalog of bright solar analogs, which could be used to calibrate activity–age–rotation relationships for stars that have long-term activity monitoring. Additionally, fast sampling will continue to enable the opportunity to constrain orbital eccentricities for small planets from transit durations and expand the sample of host stars for which asteroseismic characterization is possible. The early results presented here demonstrate the strong potential of TESS 20 second data for stellar astrophysics and exoplanet science in the first extended mission and beyond.

Data and scripts to reproduce results and figures are available on GitHub[47] and version 1.0.0 is archived in Zenodo (Huber & Ball 2021).

We thank the entire TESS team for making 20 second cadence observations possible. We also thank Zach Berta-Thompson and John Doty for helpful discussions on TESS cosmic-ray rejection algorithms and pre-flight simulations, and Kosmas Gazeas for helpful comments provided through the TASC review process.

[47] https://github.com/danxhuber/tess20sec

D.H. acknowledges support from the Alfred P. Sloan Foundation, the National Aeronautics and Space Administration (80NSSC19K0379, 80NSSC21K0652), and the National Science Foundation (AST-1717000). T.S.M. acknowledges support from NASA grant 80NSSC20K0458. Computational time at the Texas Advanced Computing Center was provided through XSEDE allocation TG-AST090107. A.C. acknowledges support from the National Science Foundation through the Graduate Research Fellowship Program (DGE 1842402). W.H. B. performed computations using the University of Birmingham's BlueBEAR High Performance Computing service. T.R. B. acknowledges support from the Australian Research Council through Discovery Project DP210103119. Funding for the Stellar Astrophysics Centre is provided by The Danish National Research Foundation (Grant DNRF106). M.S.C. and M.D. acknowledge the support by FCT/MCTES through the research grants UIDB/04434/2020, UIDP/04434/2020 and PTDC/FIS-AST/30389/2017, and by FEDER—Fundo Europeu de Desenvolvimento Regional through COMPETE2020—Programa Operacional Competitividade e Internacionalização (grant: POCI-01-0145-FEDER-030389). T.L.C. is supported by Fundação para a Ciência e a Tecnologia (FCT) in the form of a work contract (CEECIND/00476/2018). M.S.C. is supported by national funds through FCT in the form of a work contract. H. K. and E.P. acknowledge the grant from the European Social Fund via the Lithuanian Science Council (LMTLT) grant No. 09.3.3-LMT-K-712-01-0103. R.A.G. and S.N.B. acknowledge the support received from the CNES with the PLATO and GOLF grants. B.N. acknowledges postdoctoral funding from the Alexander von Humboldt Foundation and "Branco Weiss fellowship Science in Society" through the SEISMIC stellar interior physics group. S.M. acknowledges support by the Spanish Ministry of Science and Innovation with the Ramon y Cajal fellowship number RYC-2015-17697 and the grant number PID2019-107187GB-I00. T.W. acknowledges support from the B-type Strategic Priority Program of the Chinese Academy of Sciences (grant No. XDB41000000) from the NSFC of China (grant Nos. 11773064, 11873084, and 11521303), from the Youth Innovation Promotion Association of Chinese Academy of Sciences, and from the Ten Thousand Talents Program of Yunnan for Top-notch Young Talents. T.W. also gratefully acknowledges the computing time granted by the Yunnan Observatories and provided by the facilities at the Yunnan Observatories Supercomputing Platform. T.D. acknowledges support from MIT's Kavli Institute as a Kavli postdoctoral fellow.

Funding for the TESS mission is provided by NASA's Science Mission directorate. Resources supporting this work were provided by the NASA High-End Computing (HEC) Program through the NASA Advanced Supercomputing (NAS) Division at Ames Research Center for the production of the SPOC data products. This paper includes data collected by the TESS mission, which are publicly available from the Mikulski Archive for Space Telescopes (MAST).

Software: This research made use of exoplanet (Foreman-Mackey et al. 2021) and its dependencies (Agol et al. 2020; Astropy Collaboration et al. 2013, 2018, 2018; Foreman-Mackey et al. 2020; Luger et al. 2019; Salvatier et al. 2016; Theano Development Team 2016), DIAMONDS (Corsaro & De Ridder 2014), echelle (Hey & Ball 2020), exoplanet (Foreman-Mackey 2019), isoclassify (Huber et al. 2017; Berger et al. 2020), Lightkurve (Lightkurve Collaboration et al. 2018),

Matplotlib (Hunter 2007), numpy (Harris et al. 2020), and scipy (Virtanen et al. 2020).

ORCID iDs

Daniel Huber https://orcid.org/0000-0001-8832-4488
Timothy R. White https://orcid.org/0000-0002-6980-3392
Travis S. Metcalfe https://orcid.org/0000-0003-4034-0416
Ashley Chontos https://orcid.org/0000-0003-1125-2564
Michael M. Fausnaugh https://orcid.org/0000-0002-9113-7162
Cynthia S. K. Ho https://orcid.org/0000-0001-7457-5120
Vincent Van Eylen https://orcid.org/0000-0001-5542-8870
Warrick H. Ball https://orcid.org/0000-0002-4773-1017
Sarbani Basu https://orcid.org/0000-0002-6163-3472
Timothy R. Bedding https://orcid.org/0000-0001-5222-4661
Derek L. Buzasi https://orcid.org/0000-0002-1988-143X
Tiago L. Campante https://orcid.org/0000-0002-4588-5389
William J. Chaplin https://orcid.org/0000-0002-5714-8618
Jørgen Christensen-Dalsgaard https://orcid.org/0000-0001-5137-0966
Margarida S. Cunha https://orcid.org/0000-0001-8237-7343
Morgan Deal https://orcid.org/0000-0001-6774-3587
Rafael A. García https://orcid.org/0000-0002-8854-3776
Charlotte Gehan https://orcid.org/0000-0002-0833-7084
Chen Jiang https://orcid.org/0000-0002-7614-1665
Cenk Kayhan https://orcid.org/0000-0001-9198-2289
Mia S. Lundkvist https://orcid.org/0000-0002-8661-2571
Savita Mathur https://orcid.org/0000-0002-0129-0316
Mário J. P. F. G. Monteiro https://orcid.org/0000-0003-0513-8116
Benard Nsamba https://orcid.org/0000-0002-4647-2068
Jia Mian Joel Ong https://orcid.org/0000-0001-7664-648X
Aldo M. Serenelli https://orcid.org/0000-0001-6359-2769
Victor Silva Aguirre https://orcid.org/0000-0002-6137-903X
Keivan G. Stassun https://orcid.org/0000-0002-3481-9052
Tao Wu https://orcid.org/0000-0001-6832-4325
Thomas Barclay https://orcid.org/0000-0001-7139-2724
Tansu Daylan https://orcid.org/0000-0002-6939-9211
J. J. Hermes https://orcid.org/0000-0001-5941-2286
Jon M. Jenkins https://orcid.org/0000-0002-4715-9460
David W. Latham https://orcid.org/0000-0001-9911-7388
Alan M. Levine https://orcid.org/0000-0001-8172-0453
George R. Ricker https://orcid.org/0000-0003-2058-6662
Sara Seager https://orcid.org/0000-0002-6892-6948
Avi Shporer https://orcid.org/0000-0002-1836-3120
Joseph D. Twicken https://orcid.org/0000-0002-6778-7552
Roland K. Vanderspek https://orcid.org/0000-0001-6763-6562
Joshua N. Winn https://orcid.org/0000-0002-4265-047X

References

Addison, B. C., Wright, D. J., Nicholson, B. A., et al. 2021, MNRAS, 502, 3704
Aerts, C., Christensen-Dalsgaard, J., Cunha, M., & Kurtz, D. W. 2008, SoPh, 251, 3
Agol, E., Luger, R., & Foreman-Mackey, D. 2020, AJ, 159, 123
Aguilera-Gómez, C., Ramírez, I., & Chanamé, J. 2018, A&A, 614, A55
Albrecht, S., Winn, J. N., Johnson, J. A., et al. 2012, ApJ, 757, 18
Antia, H. M., & Basu, S. 1994, A&As, 107, 421
Appourchaux, T., Benomar, O., Gruberbauer, M., et al. 2012, A&A, 537, A134
Astropy Collaboration, Robitaille, T. P., Tollerud, E. J., et al. 2013, A&A, 558, A33
Astropy Collaboration, Price-Whelan, A. M., Sipőcz, B. M., et al. 2018, AJ, 156, 123
Baglin, A., Michel, E., Auvergne, M. & The COROT Team 2006, Proc. of The CoRoT Mission Pre-Launch Status - Stellar Seismology and Planet Finding, ESA SP-1306 (Noordwijk: ESA)
Baliunas, S. L., Donahue, R. A., Soon, W. H., et al. 1995, ApJ, 438, 269
Ball, W. H., & Gizon, L. 2014, A&A, 568, A123
Ball, W. H., & Gizon, L. 2017, A&A, 600, A128
Ball, W. H., Chaplin, W. J., Nielsen, M. B., et al. 2020, MNRAS, 499, 6084
Ballard, S., Chaplin, W. J., Charbonneau, D., et al. 2014, ApJ, 790, 12
Ballot, J., García, R. A., & Lambert, P. 2006, MNRAS, 369, 1281
Barnes, S. A. 2003, ApJ, 586, 464
Basu, S., Chaplin, W. J., & Elsworth, Y. 2010, ApJ, 710, 1596
Becker, J. C., Vanderburg, A., Rodriguez, J. E., et al. 2019, AJ, 157, 19
Bedding, T. R., Kjeldsen, H., Arentoft, T., et al. 2007, ApJ, 663, 1315
Bell, K. J., Córsico, A. H., Bischoff-Kim, A., et al. 2019, A&A, 632, A42
Benomar, O., Baudin, F., Chaplin, W. J., Elsworth, Y., & Appourchaux, T. 2012, MNRAS, 420, 2178
Benomar, O., Masuda, K., Shibahashi, H., & Suto, Y. 2014, PASJ, 66, 94
Bensby, T., Feltzing, S., Lundström, I., & Ilyin, I. 2005, A&A, 433, 185
Berger, T. A., Huber, D., Gaidos, E., van Saders, J. L., & Weiss, L. M. 2020, AJ, 160, 108
Boro Saikia, S., Marvin, C. J., Jeffers, S. V., et al. 2018, A&A, 616, A108
Borucki, W., Koch, D., Basri, G., et al. 2008, in IAU Symp. 249, Exoplanets: Detection, Formation and Dynamics, ed. Y.-S. Sun, S. Ferraz-Mello, & J.-L. Zhou (Cambridge: Cambridge Univ. Press), 17
Bouchy, F., Bazot, M., Santos, N. C., Vauclair, S., & Sosnowska, D. 2005, A&A, 440, 609
Brown, T. M., Gilliland, R. L., Noyes, R. W., & Ramsey, L. W. 1991, ApJ, 368, 599
Campante, T. L. 2018, Asteroseismology and Exoplanets: Listening to the Stars and Searching for New Worlds, Vol. 49 (Berlin: Springer), 55
Campante, T. L., Barclay, T., Swift, J. J., et al. 2015, ApJ, 799, 170
Campante, T. L., Schofield, M., Kuszlewicz, J. S., et al. 2016, ApJ, 830, 138
Campante, T. L., Corsaro, E., Lund, M. N., et al. 2019, ApJ, 885, 31
Casagrande, L., Schönrich, R., Asplund, M., et al. 2011, A&A, 530, A138
Casagrande, L., Silva Aguirre, V., Schlesinger, K. J., et al. 2016, MNRAS, 455, 987
Çelik Orhan, Z., Yıldız, M., & Kayhan, C. 2021, MNRAS, 503, 4529
Chaplin, W. J., Elsworth, Y., Davies, G. R., et al. 2014, MNRAS, 445, 946
Chaplin, W. J., Sanchis-Ojeda, R., Campante, T. L., et al. 2013, ApJ, 766, 101
Charpinet, S., Brassard, P., Fontaine, G., et al. 2019, A&A, 632, A90
Chatterjee, S., Ford, E. B., Matsumura, S., & Rasio, F. A. 2008, ApJ, 686, 580
Choi, J., Dotter, A., Conroy, C., et al. 2016, ApJ, 823, 102
Chontos, A., Huber, D., Sayeed, M., & Yamsiri, P. 2021a, arXiv:2108.00582
Chontos, A., Huber, D., Latham, D. W., et al. 2019, AJ, 157, 192
Chontos, A., Huber, D., Kjeldsen, H., et al. 2021b, ApJ, 922, 229
Christensen-Dalsgaard, J. 1988, in Proc. IAU Symp. 123, Advances in Helio- and Asteroseismology, ed. J. Christensen-Dalsgaard & S. Frandsen (Dordrecht: Kluwer)
Christensen-Dalsgaard, J. 2008, Ap&SS, 316, 13
Christensen-Dalsgaard, J., Silva Aguirre, V., Elsworth, Y., & Hekker, S. 2014, MNRAS, 445, 3685
Cloutier, R., & Menou, K. 2020, AJ, 159, 211
Corsaro, E., & De Ridder, J. 2014, A&A, 571, A71
Corsaro, E., De Ridder, J., & García, R. A. 2015, A&A, 579, A83
Cossou, C., Raymond, S. N., Hersant, F., & Pierens, A. 2014, A&A, 569, A56
Creevey, O. L., Metcalfe, T. S., Schultheis, M., et al. 2017, A&A, 601, A67
Damasso, M., Sozzetti, A., Lovis, C., et al. 2020, A&A, 642, A31
Davenport, J. R. A. 2016, ApJ, 829, 23
David, T. J., Contardo, G., Sandoval, A., et al. 2021, AJ, 161, 265
Davies, G. R., Silva Aguirre, V., Bedding, T. R., et al. 2016, MNRAS, 456, 2183
Dawson, R. I., & Johnson, J. A. 2012, ApJ, 756, 122
De Rosa, R. J., Dawson, R., & Nielsen, E. L. 2020, A&A, 640, A73
Demarque, P., Guenther, D. B., Li, L. H., Mazumdar, A., & Straka, C. W. 2008, Ap&SS, 316, 31
Escobar, M. E., Théado, S., Vauclair, S., et al. 2012, A&A, 543, A96
Fabrycky, D., & Tremaine, S. 2007, ApJ, 669, 1298
Feinstein, A. D., Montet, B. T., Ansdell, M., et al. 2020, AJ, 160, 219
Foreman-Mackey, D. 2019, Exoplanet: Probabilistic Modeling of Transit or Radial Velocity Observations of Exoplanets, Astrophysics Source Code Library, ascl:1910.005
Foreman-Mackey, D., Luger, R., Czekala, I., et al. 2020, exoplanet-dev/exoplanet v0.4.0, doi:10.5281/zenodo.1998447
Foreman-Mackey, D., Luger, R., Agol, E., et al. 2021, JOSS, 6, 3285
Fulton, B. J., & Petigura, E. A. 2018, AJ, 156, 264
Fulton, B. J., Petigura, E. A., Howard, A. W., et al. 2017, AJ, 154, 109
Gai, N., Basu, S., Chaplin, W. J., & Elsworth, Y. 2011, ApJ, 730, 63
Gaia Collaboration, Prusti, T., de Bruijne, J. H. J., et al. 2016, A&A, 595, A1
Gandolfi, D., Barragán, O., Livingston, J. H., et al. 2018, A&A, 619, L10

García, R. A., & Ballot, J. 2019, LRSP, 16, 4
García, R. A., Régulo, C., Samadi, R., et al. 2009, A&A, 506, 41
García Muñoz, A., Fossati, L., Youngblood, A., et al. 2021, ApJL, 907, L36
García Muñoz, A., Youngblood, A., Fossati, L., et al. 2020, ApJL, 888, L21
Gilliland, R. L., Jenkins, J. M., Borucki, W. J., et al. 2010, ApJL, 713, L160
Ginzburg, S., Schlichting, H. E., & Sari, R. 2018, MNRAS, 476, 759
Gizon, L., & Solanki, S. K. 2003, ApJ, 589, 1009
Goldreich, P., & Soter, S. 1966, Icar, 5, 375
Grec, G., Fossat, E., & Pomerantz, M. A. 1983, SoPh, 82, 55
Günther, M. N., & Daylan, T. 2021, ApJS, 254, 13
Günther, M. N., Zhan, Z., Seager, S., et al. 2020, AJ, 159, 60
Gupta, A., & Schlichting, H. E. 2020, MNRAS, 493, 792
Handberg, R., & Campante, T. L. 2011, A&A, 527, A56
Handler, G. 2013, in Asteroseismology, ed. T. D. Oswalt & M. A. Barstow, Vol. 4 (Berlin: Springer), 207
Hardegree-Ullman, K. K., Zink, J. K., Christiansen, J. L., et al. 2020, ApJS, 247, 28
Harris, C. R., Millman, K. J., van der Walt, S. J., et al. 2020, Natur, 585, 357
Harvey, J. W. 1988, in IAU Symp. 123, Advances in Helio- and Asteroseismology, ed. J. Christensen-Dalsgaard & S. Frandsen (Dordrecht: Reidel), 497
Hawley, S. L., Davenport, J. R. A., Kowalski, A. F., et al. 2014, ApJ, 797, 121
Hekker, S., Elsworth, Y., De Ridder, J., et al. 2011, A&A, 525, A131
Hey, D., & Ball, W. 2020, Echelle: Dynamic echelle diagrams for asteroseismology, v1.4, Zenodo, doi:10.5281/zenodo.3629933
Høg, E., Fabricius, C., Makarov, V. V., et al. 2000, A&A, 355, L27
Howell, S. B., Sobeck, C., Haas, M., et al. 2014, PASP, 126, 398
Huang, C. X., Burt, J., Vanderburg, A., et al. 2018, ApJL, 868, L39
Huber, D., & Ball, W. 2021, danxhuber/tess20sec: v1.0.0, Zenodo, doi:10.5281/zenodo.5555456
Huber, D., Stello, D., Bedding, T. R., et al. 2009, CoAst, 160, 74
Huber, D., Chaplin, W. J., Christensen-Dalsgaard, J., et al. 2013a, ApJ, 767, 127
Huber, D., Carter, J. A., Barbieri, M., et al. 2013b, Sci, 342, 331
Huber, D., Bryson, S. T., Haas, M. R., et al. 2017, ApJ, 224, 2
Huber, D., Chaplin, W. J., Chontos, A., et al. 2019, AJ, 157, 245
Hunter, J. D. 2007, CSE, 9, 90
Hut, P. 1981, A&A, 99, 126
Jenkins, J. M., Caldwell, D. A., Chandrasekaran, H., et al. 2010, ApJL, 713, L120
Jenkins, J. M., Twicken, J. D., McCauliff, S., et al. 2016, Proc. SPIE, 9913, 99133E
Jones, H. R. A., Paul Butler, R., Tinney, C. G., et al. 2002, MNRAS, 333, 871
Kamiaka, S., Benomar, O., & Suto, Y. 2018, MNRAS, 479, 391
Kamiaka, S., Benomar, O., Suto, Y., et al. 2019, AJ, 157, 137
Kayhan, C., Yıldız, M., & Çelik Orhan, Z. 2019, MNRAS, 490, 1509
Kjeldsen, H., Bedding, T. R., & Christensen-Dalsgaard, J. 2008, ApJL, 683, L175
Kjeldsen, H., Bedding, T. R., Butler, R. P., et al. 2005, ApJ, 635, 1281
Kozai, Y. 1962, AJ, 67, 591
Kunovac Hodžić, V., Triaud, A. H. M. J., Cegla, H. M., Chaplin, W. J., & Davies, G. R. 2021, MNRAS, 502, 2893
Lebreton, Y. 2012, in ASP Conf. Ser., 462, Progress in Solar/Stellar Physics with Helio- and Asteroseismology, ed. H. Shibahashi, M. Takata, & A. E. Lynas-Gray (San Francisco, CA: ASP), 469
Lebreton, Y., & Goupil, M. J. 2014, A&A, 569, A21
Lenz, P., & Breger, M. 2005, CoAst, 146, 53
Lidov, M. L. 1962, P&SS, 9, 719
Lightkurve Collaboration, Cardoso, J. V. D. M., Hedges, C., et al. 2018, Lightkurve: Kepler and TESS time series analysis in Python, Astrophysics Source Code Library, ascl:1812.013
Lindegren, L., Klioner, S. A., Hernández, J., et al. 2021, A&A, 649, A2
Lissauer, J. J., Fabrycky, D. C., Ford, E. B., et al. 2011, Natur, 470, 53
Lorenzo-Oliveira, D., Freitas, F. C., Meléndez, J., et al. 2018, A&A, 619, A73
Luger, R., Agol, E., Foreman-Mackey, D., et al. 2019, AJ, 157, 64
Lund, M. N., Lundkvist, M., Silva Aguirre, V., et al. 2014, A&A, 570, A54
Lund, M. N., Knudstrup, E., Silva Aguirre, V., et al. 2019, AJ, 158, 248
Lundkvist, M. S. 2015, PhD Thesis, Aarhus University, Denmark
Lundkvist, M. S., Kjeldsen, H., Albrecht, S., et al. 2016, NatCo, 7, 11201
Mamajek, E. E., & Hillenbrand, L. A. 2008, ApJ, 687, 1264
Mathis, S. 2018, in Handbook of Exoplanets, ed. H. J. Deeg & J. A. Belmonte (Berlin: Springer), 24
Mathur, S., García, R. A., Régulo, C., et al. 2010, A&A, 511, A46
Matthews, J. M., Kusching, R., Guenther, D. B., et al. 2004, Natur, 430, 51
Metcalfe, T. S., Creevey, O. L., & Christensen-Dalsgaard, J. 2009, ApJ, 699, 373
Metcalfe, T. S., Chaplin, W. J., Appourchaux, T., et al. 2012, ApJL, 748, L10
Metcalfe, T. S., van Saders, J. L., Basu, S., et al. 2020, ApJ, 900, 154
Metcalfe, T. S., van Saders, J. L., Basu, S., et al. 2021, ApJ, 921, 122
Mosser, B., & Appourchaux, T. 2009, A&A, 508, 877
Mosser, B., Deheuvels, S., Michel, E., et al. 2008, A&A, 488, 635
Mosser, B., Elsworth, Y., Hekker, S., et al. 2012a, A&A, 537, A30
Mosser, B., Goupil, M. J., Belkacem, K., et al. 2012b, A&A, 548, A10
Mosumgaard, J. R., Ball, W. H., Silva Aguirre, V., Weiss, A., & Christensen-Dalsgaard, J. 2018, MNRAS, 478, 5650
Murphy, S. J., Shibahashi, H., & Kurtz, D. W. 2013, MNRAS, 430, 2986
Nagasawa, M., Ida, S., & Bessho, T. 2008, ApJ, 678, 498
Nielsen, M. B., Ball, W. H., Standing, M. R., et al. 2020, A&A, 641, A25
Nielsen, M. B., Davies, G. R., Ball, W. H., et al. 2021, AJ, 161, 62
Ogilvie, G. I. 2014, ARA&A, 52, 171
Ong, J. M. J., Basu, S., & McKeever, J. M. 2021, ApJ, 906, 54
Owen, J. E., & Wu, Y. 2017, ApJ, 847, 29
Paxton, B., Bildsten, L., Dotter, A., et al. 2011, ApJS, 192, 3
Paxton, B., Cantiello, M., Arras, P., et al. 2013, ApJS, 208, 4
Paxton, B., Marchant, P., Schwab, J., et al. 2015, ApJS, 220, 15
Petigura, E. A. 2020, AJ, 160, 89
Price, E. M., & Rogers, L. A. 2014, ApJ, 794, 92
Pu, B., & Lai, D. 2019, MNRAS, 488, 3568
Reegen, P., Kallinger, T., Frast, D., et al. 2006, MNRAS, 367, 1417
Rendle, B. M., Buldgen, G., Miglio, A., et al. 2019, MNRAS, 484, 771
Ricker, G. R., Winn, J. N., Vanderspek, R., et al. 2014, Proc. SPIE, 9143, 914320
Rodrigues, T. S., Girardi, L., Miglio, A., et al. 2014, MNRAS, 445, 2758
Rodrigues, T. S., Bossini, D., Miglio, A., et al. 2017, MNRAS, 467, 1433
Rubenzahl, R. A., Dai, F., Howard, A. W., et al. 2021, AJ, 161, 119
Saar, S. H., & Testa, P. 2012, in IAU Symp. 286, Comparative Magnetic Minima: Characterizing Quiet Times in the Sun and Stars, ed. C. H. Mandrini & D. F. Webb (Cambridge: Cambridge Univ. Press), 335
Salabert, D., García, R. A., Beck, P. G., et al. 2016, A&A, 596, A31
Salaris, M., Chieffi, A., & Straniero, O. 1993, ApJ, 414, 580
Salvatier, J., Wiecki, T. V., & Fonnesbeck, C. 2016, PeerJ Comp. Sci., 2, e55
Sandoval, A., Contardo, G., & David, T. J. 2021, ApJ, 911, 117
Savitzky, A., & Golay, M. J. E. 1964, AnaCh, 36, 1627
Schofield, M., Chaplin, W. J., Huber, D., et al. 2019, ApJS, 241, 12
Seager, S., & Mallén-Ornelas, G. 2003, ApJ, 585, 1038
Serenelli, A., Johnson, J., Huber, D., et al. 2017, ApJS, 233, 23
Silva Aguirre, V., Davies, G. R., Basu, S., et al. 2015, MNRAS, 452, 2127
Silva Aguirre, V., Lund, M. N., Antia, H. M., et al. 2017, ApJ, 835, 173
Silva Aguirre, V., Bojsen-Hansen, M., Slumstrup, D., et al. 2018, MNRAS, 475, 5487
Smith, J. C., Stumpe, M. C., Van Cleve, J. E., et al. 2012, PASP, 124, 1000
Stassun, K. G., & Torres, G. 2016, AJ, 152, 180
Stassun, K. G., Oelkers, R. J., Pepper, J., et al. 2018, AJ, 156, 102
Stassun, K. G., Oelkers, R. J., Paegert, M., et al. 2019, AJ, 158, 138
Stello, D., Chaplin, W. J., Bruntt, H., et al. 2009, ApJ, 700, 1589
Stello, D., Zinn, J., Elsworth, Y., et al. 2017, ApJ, 835, 83
Stello, D., Saunders, N., Grunblatt, S., et al. 2021, arXiv:2107.05831
Stumpe, M. C., Smith, J. C., Catanzarite, J. H., et al. 2014, PASP, 126, 100
Stumpe, M. C., Smith, J. C., Van Cleve, J. E., et al. 2012, PASP, 124, 985
Sullivan, P. W., Winn, J. N., Berta-Thompson, Z. K., et al. 2015, ApJ, 809, 77
Tayar, J., Claytor, Z. R., Huber, D., & van Saders, J. 2020, arXiv:2012.07957
Teixeira, T. C., Kjeldsen, H., Bedding, T. R., et al. 2009, A&A, 494, 237
Theano Development Team 2016, arXiv:1605.02688
Tobie, G., Grasset, O., Dumoulin, C., & Mocquet, A. 2019, A&A, 630, A70
Torres, G., Fischer, D. A., Sozzetti, A., et al. 2012, ApJ, 757, 161
Townsend, R. H. D., & Teitler, S. A. 2013, MNRAS, 435, 3406
Ulrich, R. K. 1986, ApJL, 306, L37
Van Eylen, V., Agentoft, C., Lundkvist, M. S., et al. 2018a, MNRAS, 479, 4786
Van Eylen, V., & Albrecht, S. 2015, ApJ, 808, 126
Van Eylen, V., Dai, F., Mathur, S., et al. 2018b, MNRAS, 478, 4866
Van Eylen, V., Albrecht, S., Huang, X., et al. 2019, AJ, 157, 61
Van Eylen, V., Astudillo-Defru, N., Bonfils, X., et al. 2021, MNRAS, 507, 2154
van Saders, J. L., Ceillier, T., Metcalfe, T. S., et al. 2016, Natur, 529, 181
Vanderburg, A., Becker, J. C., Kristiansen, M. H., et al. 2016, ApJL, 827, L10
Vanderburg, A., Rappaport, S. A., Xu, S., et al. 2020, Natur, 585, 363
Vanderspek, R., Doty, J., Fausnaugh, M., et al. 2018, TESS Instrument Handbook (Washington, DC: TESS), https://archive.stsci.edu/missions/tess/doc/TESS_Instrument_Handbook_v0.1.pdf
Vauclair, S., Laymand, M., Bouchy, F., et al. 2008, A&A, 482, L5
Verner, G. A., Elsworth, Y., Chaplin, W. J., et al. 2011, MNRAS, 415, 3539

Virtanen, P., Gommers, R., Oliphant, T. E., et al. 2020, NatMe, 17, 261
Wahr, J. M. 1981, GeoJ, 64, 677
Walker, G., Matthews, J., Kuschnig, R., et al. 2003, PASP, 115, 1023
Weiss, W. W., Moffat, A. F. J., & Kudelka, O. 2008, CoAst, 157, 271
Weiss, W. W., Rucinski, S. M., Moffat, A. F. J., et al. 2014, PASP, 126, 573
White, T. R., Bedding, T. R., Stello, D., et al. 2011, ApJ, 743, 161
White, T. R., Huber, D., Mann, A. W., et al. 2018, MNRAS, 477, 4403
Winn, J. N., Fabrycky, D., Albrecht, S., & Johnson, J. A. 2010, ApJL, 718, L145
Xie, J.-W., Dong, S., Zhu, Z., et al. 2016, PNAS, 113, 11431
Xuan, J. W., & Wyatt, M. C. 2020, MNRAS, 497, 2096
Zhang, J., Weiss, L. M., Huber, D., et al. 2021, AJ, 162, 89
Zinn, J. C., Pinsonneault, M. H., Huber, D., et al. 2019, ApJ, 885, 166
Zinn, J. C., Stello, D., Elsworth, Y., et al. 2020, ApJS, 251, 23